Inorganic Chemistry

Article

Cite This: Inorg. Chem. XXXX, XXX, XXX–XXX

pubs.acs.org/IC

# Second-Sphere Effects in Dinuclear $Fe^{III}Zn^{II}$ Hydrolase Biomimetics: Tuning Binding and Reactivity Properties

Tiago Pacheco Camargo,[†] Ademir Neves,*[,†] Rosely A. Peralta,[†] Cláudia Chaves,[†] Elene C. P. Maia,[‡] Edgar H. Lizarazo-Jaimes,[‡] Dawidson A. Gomes,[§] Tiago Bortolotto,[⊥] Douglas R. Norberto,[⊥] Hernán Terenzi,*[,⊥] David L. Tierney,[∥] and Gerhard Schenk[#]

[†]Departamento de Química, LABINC, and [⊥]Departamento de Bioquímica, CEBIME, Universidade Federal de Santa Catarina, Florianópolis, Santa Catarina 88040-900, Brazil

[‡]Departamento de Química and [§]Departamento de Bioquímica, Universidade Federal de Minas Gerais, Belo Horizonte, Minas Gerais 31270-901, Brazil

[∥]Department of Chemistry and Biochemistry, Miami University, Oxford, Ohio 45056, United States,

[#]School of Chemistry and Molecular Biosciences, The University of Queensland, Brisbane 4072, Australia

Supporting Information

**ABSTRACT:** Herein, we report the synthesis and characterization of two dinuclear $Fe^{III}Zn^{II}$ complexes $[Fe^{III}Zn^{II}LP1]$ (**1**) and $[Fe^{III}Zn^{II}LP2]$ (**2**), in which LP1 and LP2 are conjugated systems containing one and two pyrene groups, respectively, connected via the diamine $-HN(CH_2)_4NH-$ spacer to the well-known $N_5O_2$-donor $H_2L$ ligand ($H_2L$ = 2-bis{[(2-pyridylmethyl)aminomethyl]-6-[(2-hydroxybenzyl)(2-pyridylmethyl)]aminomethyl}-4-methylphenol). The complex $[Fe^{III}Zn^{II}L1]$ (**3**), in which $H_2L$ was modified to $H_2L1$, with a carbonyl group attached to the terminal phenol group, was included in this study for comparison purposes.[1] Both complexes **1** and **2** were satisfactorily characterized in the solid state and in solution. Extended X-ray absorption fine structure data for **1** and **3** in an acetonitrile solution show that the multiply bridged structure seen in the solid state of **3** is retained in solution. Potentiometric and UV−vis titration of **1** and **2** show that electrostatic interaction between the protonated amino groups and coordinated water molecules significantly decreases the $pK_a$ of the iron(III)-bound water compared to those of **3**. On the other hand, catalytic activity studies using **1** and **2** in the hydrolysis of the activated substrate bis(2,4-dinitrophenyl)phosphate (BDNPP) resulted in a significant increase in the association of the substrate ($K_{ass} \cong 1/K_M$) compared to that of **3** because of electrostatic and hydrophobic interactions between BDNPP and the side-chain diaminopyrene of the ligands $H_2LP1$ and $H_2LP2$. In addition, the introduction of the pyrene motifs in **1** and **2** enhanced their activity toward DNA and as effective antitumor drugs, although the biochemical mechanism of the latter effect is currently under investigation. These complexes represent interesting examples of how to promote an increase in the activity of traditional artificial metal nucleases by introducing second-coordination-sphere effects.

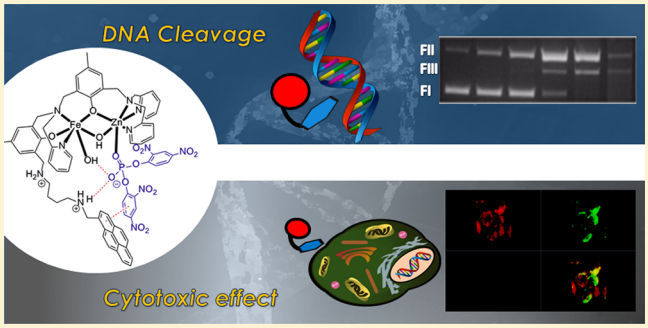


## INTRODUCTION

Model complexes capable of cleaving phosphate ester bonds have been attracting increasing interest in view of both their importance at a fundamental level (e.g., as a biomimetic system to elucidate the structure and mechanism of corresponding enzymes) and their potential as new therapeutic drugs targeting specific types of DNA or RNA (so-called "catalytic drugs") and antibiotics.[2] However, although synthetic model complexes are capable of mimicking the structural and physicochemical properties, and frequently mechanistic aspects, of the corresponding active sites of their biological counterparts, the catalytic efficiency of the metalloenzymes remains largely unrivaled.[3,4]

Indeed, the absence of a well-defined binding site that provides relevant contact points for noncovalent interactions between the model system and the reactants in model systems is to a large extent responsible for the discrepancy of the catalytic efficiency between biomimetics and true enzymes.[5] As a consequence, attempts to generate model complexes that may mimic hydrogen-bonding and electrostatic interactions, as well as hydrophobic effects and van der Waals forces, have recently gained momentum.[5] Specifically, among the strategies used to increase the hydrolytic efficiency and selectivity of artificial metal-ion-dependent hydrolytic systems, complexes modified with noncoordinating functional groups such as amines, guanidines, and hybrid mimics such as polyethylene imines, dendrimers, and gold nanoparticles have been reported.[5−8] Cyclodextrins and calix[*n*]arene-containing polypeptides, in

Received: September 19, 2017




DOI: 10.1021/acs.inorgchem.7b02384
Inorg. Chem. XXXX, XXX, XXX−XXX

which the biomimetic complex is covalently linked to the supramolecular hosts, have also been described.[5,6]

The major functions of the second coordination sphere of metallohydrolases are related to the activation of both the metal-bound nucleophilic water ($H_2O$)/$OH^-$ and the substrate, as well as stabilization of the transition state (TS).[5] Aliphatic amines are particularly interesting in this case because they tend to be protonated in solution (relevant p$K_a$ values are comparable to that of lysine), and thus they may contribute to electrostatic interactions. However, only a few examples of such biomimetics have been described to date. Structural evidence for the interaction between positively charged ammonium groups and the substrate mimic phenylphosphate has been reported for a dinuclear copper complex by Kövári and Krämer.[9] The X-ray structure of this complex indicated the presence of a hydrogen bond between the tertiary ammonium moiety of the bipyridine ligand and the metal-bridging phosphoryl group of the substrate mimic. A dinuclear [$Fe^{III}$($\mu$-oxo)$Fe^{III}$] (Figure 1) core containing

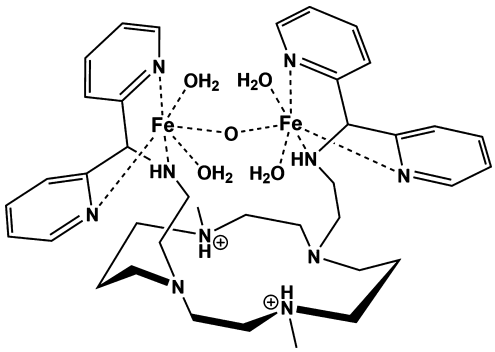


**Figure 1.** Structure of the $[(H_2L_x)\{Fe^{III}_2\text{-}O\}(Cl)_4]^{2+}$ complex containing a cyclam group as an anchor.

a protonated 1,4,8,11-tetraazacyclotetradecane (cyclam) platform has been reported as a functional model for the metallohydrolase purple acid phosphatase (PAP), catalyzing the hydrolysis of the activated phosphomonoester 2,4-dinitrophenyl phosphate (DNPP).[10] Secondary effects exerted by such a protonated cyclam platform have been proposed as being responsible for the positioning and activation of the monodentately iron(III)-bound substrate.[11]

The design of small molecules able to cleave DNA under physiological conditions is of great interest for the development of novel therapeutic agents. Considerable effort has been invested in preparing metal complexes capable of binding and breaking the DNA double helix.[2] However, there are only a few examples of hydrolytically active metal complexes that have been linked to DNA intercalating groups.[12] In 1987, Barton and co-workers reported the first example of an artificial DNA-intercalating system with hydrolytic activity toward DNA.[12] The system consisted of an intercalating ruthenium tris-(phenanthroline) derivative attached to two bis(aminoethyl)-amine (dien) moieties for complexing metal ions. The dinuclear zinc(II) complex of this ligand cleaves ca. 40% of plasmid DNA in 5 h at 37 °C and pH 8.5, with a rate constant of ~$3 \times 10^{-5}$ $s^{-1}$. This remarkably high rate for a zinc(II) complex may be due to intercalation, although no direct evidence to support this hypothesis has been reported. Schneider and co-workers[13] reported an europium(III) complex containing two naphthalene groups anchored to an azacrown ligand via C6 alkyl spacers as an efficient DNA cleaving agent. However, while the catalytic activity ($k_{cat}$) increased by around a factor of 10 in comparison to that of europium(III) alone, the 15-fold increase of the Michaelis−Menten constant, $K_M$, was unexpected, given that intercalation of naphthylalkylamines into double-stranded DNA (dsDNA) has been unequivocally established and thus the affinity of the catalyst for nucleic acid should be enhanced.[13] In a zinc(II)-containing heptapeptide complex, the introduction of an acridine moiety at the N-terminus of the peptide resulted in a slight increase in the activity at low catalyst concentrations, compensated for by a decrease at higher concentrations due to the formation of dimers or larger aggregates of the peptide induced by the presence of the acridine moiety in association with the amphiphilic character of the helix.[14] More remarkable in this context is a diiron$^{III}$ complex bearing two acridine intercalators, which shows a DNA hydrolytic cleavage rate of $6.6 \times 10^{-3}$ $s^{-1}$ at 37 °C and pH 7.0. This value represents a 300-fold rate acceleration compared to the same complex without the acridine groups and a 14-fold acceleration relative to the complex bearing only a single acridine group.[15] Another relevant example was reported by Tonellato and co-workers.[16] These authors studied the activity of a series of zinc(II) *cis*-1,3,5-triaminocyclohexane ($Zn^{II}$-tach)/anthraquinone intercalators linked with alkyl spacers of varying length (C4−C8) in the cleavage of plasmid DNA. Two important observations were made. First, the complex containing the C8 alkyl spacer cleaves supercoiled DNA 15-fold more efficiently than the simple $Zn^{II}$-tach complex without the anthraquinone moiety. Second, for the shorter spacer (C4), no cleavage could be observed, indicating that the advantage derived from increased DNA affinity is canceled out by the incorrect positioning of the reactive group. Hence, from the examples presented above, it emerges that, apart from the hydrolytic active site, the nature of the intercalator as well as the type and size of the spacer between the catalytic center and the intercalator plays a major role in the reactivity of such conjugated systems.

Guided by the structure and physicochemical properties of PAPs, our group has reported a great variety of mixed-valent $M^{III}M^{II}$ complexes ($M^{III}$ = Fe, Ga; $M^{II}$= Fe, Zn, Cu, Ni, Mn, Co, Hg, Cd) with the unsymmetrical ligand $H_2L$ = 2-bis{[(2-pyridylmethyl)aminomethyl]-6-[(2-hydroxybenzyl)(2-pyridylmethyl)]aminomethyl}-4-methylphenol as functional and structural models for the active site of these enzymes.[1,4,17−24]

Of particular relevance with regard to these $M^{III}M^{II}L$ biomimetics is the fact that the dinuclear catalyst contains a labile $M^{II}$-$OH_2$ site for monodentate substrate binding and an adjacent $M^{III}$-OH group as the initiating nucleophile that can be generated at pH values close to 7.0.[21] Additionally, the mechanism of phosphate diester bond cleavage in the DNA model substrate bis(2,4-dinitrophenyl)phosphate (BDNPP) and in DNA itself by these complexes is well established.[20,21] Herein, in an attempt to generate more efficient and selective catalysts for dsDNA cleavage, we describe a modification of these model systems by connecting a pyrene structural unit via the diamine −HN$(CH_2)_4$NH− spacer to the well-characterized $Fe^{III}Zn^{II}L$ complex.[1] In this complex, the ligand $H_2L$ was modified to 2-bis{[(2-pyridylmethyl)aminomethyl]-6-[*N*-(2-pyridylmethyl)-aminomethyl]}-4-methyl-6-formylphenol ($H_2L1$), with a carbonyl group attached to the terminal phenol group, which is ideally oriented for further chemical modifications. This $H_2L1$ ligand was used for the synthesis of the conjugated systems 2-{[bis(pyridin-2-ylmethyl)amino]methyl}-6-{[[[2-hydroxy-5-methyl-3-[[[4-[(pyren-1-ylmethyl)amino]butyl]amino]-methyl]phenyl]methyl](pyridin-2-ylmethyl)amino]methyl}-4-


DOI: 10.1021/acs.inorgchem.7b02384
*Inorg. Chem.* XXXX, XXX, XXX−XXX

**Chart 1. Proposed Structures for 1 and 2**

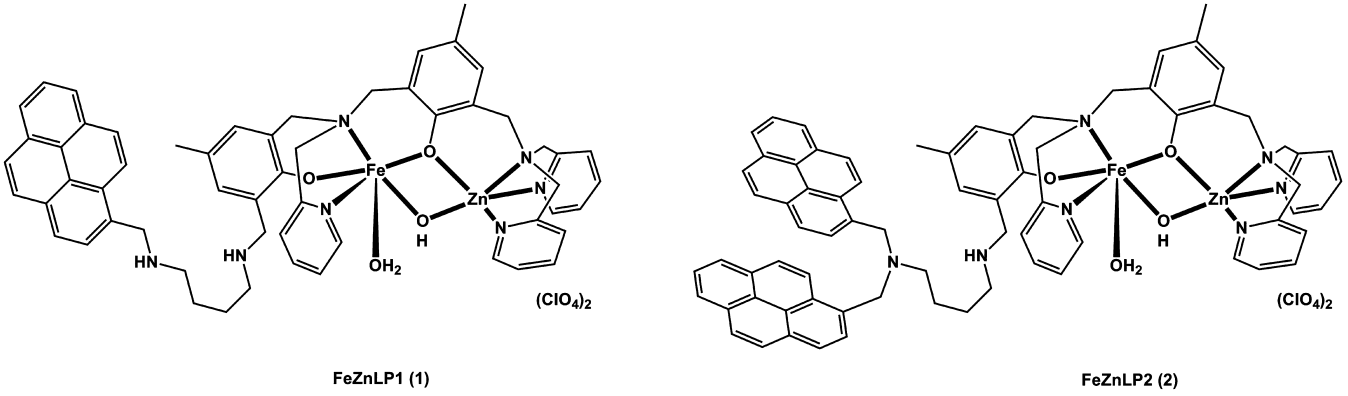


methylphenol ($H_2$LP1) and 2-{[[[3-[[[4-[bis(pyren-1-ylmethyl)amino]butyl]amino]methyl]-2-hydroxy-5-methylphenyl]methyl](pyridin-2-ylmethyl)amino]methyl}-6-{[bis(pyridin-2-ylmethyl)amino]methyl}-4-methylphenol ($H_2$LP2) and their corresponding $Fe^{III}Zn^{II}$ complexes (Chart 1). The diesterase activity (using the model substrate BDNPP and DNA) and cytotoxic activity are significantly increased because of the presence of protonated amines and conjugated pyrene(s) in the [$Fe^{III}Zn^{II}$LP1] (**1**) and [$Fe^{III}Zn^{II}$LP2] (**2**) catalysts. When DNA was used as the substrate, we observed an important increase in the cleavage activity in complexes containing pyrene groups. Interestingly, using a footprinting technique, the contact points of the three complexes on the DNA double-helix surface were established, and then the ability of the complex containing two pyrene moieties to protect a larger DNA surface was demonstrated. Confocal fluorescence microscopy reveals that complex **1** accumulates in the lysosomes of mammalian cells, as previously shown for other metal complexes, which, in addition to their DNA interacting properties, suggests its potential as a novel lead for antitumor drugs.

## EXPERIMENTAL SECTION

**Materials and Methods.** All starting materials were purchased from Aldrich, Acros, or Merck. The plasmid pBSK II (2961 bp, purchased from Stratagene California, San Diego, CA) was used as a substrate for DNA cleavage assays. The plasmid was transformed into DH5$\alpha$ *Escherichia coli* competent cells, amplified as previously described,[25] and then purified from *E. coli* cells according to the manufacturer's instructions (Qiagen Plasmid Maxi Kit protocol). The self-complementary 49-mer oligonucleotide (5′-FAM-CCG ATT ATT TAA TCG CCG GCC GC*T TTT T*GC GGC CGG CGA TTA AAT AAT C-3′, where FAM is fluorescein and the thymine nucleotides, shown in italics, represent the predicted hairpin loop) used in DNase I footprinting assays was purchased from IDT (Coralville, IA) and used without further purification. DNase I (from bovine pancreas, type IV, lyophilized powder, ≥2000 Kunitz units/mg of protein) was purchased from Sigma-Aldrich (St. Louis, MO), resuspended in 2.5 mM $CaCl_2$ and 5 mM $MgCl_2$ at 0.03 units of DNase I/$\mu$L, and stored at −20 °C. $^1$H NMR spectra were recorded with a Bruker FT 200 MHz instrument at room temperature and the chemical shifts referenced to the residual solvent ($CDCl_3$) signal. IR spectra were recorded with a PerkinElmer FTIR Spectrum 100 spectrophotometer (KBr pellets). Elemental analysis was performed on a Carlo Erba E-1110 analyzer. Electronic absorption spectra in the 200−1200 nm range were recorded on a PerkinElmer Lambda 750 spectrophotometer. Electrochemical measurements were obtained using a BAS Epsilon potentiostat/galvanostat. Cyclic voltammograms were obtained for the complexes in an acetonitrile ($CH_3CN$)/$H_2O$ (2:1) solution containing 0.1 M sodium tetrafluoroborate as the supporting electrolyte under an argon atmosphere. The electrochemical cell employed was of a standard three-electrode configuration: a glassy carbon (working), a platinum wire (counter), and Ag/$Ag^+$ (reference). Potassium hexacyanoferrate(III) ($E_{1/2}$ = 369 mV vs NHE) was used as the internal standard.[26] Electrospray ionization mass spectrometry (ESI-MS) of the complexes dissolved in an ultrapure $CH_3CN$ solution (500 nM) was performed using an AmaZon X Ion Trap MS instrument (Bruker Daltonics) with an ion-spray source using electrospray ionization in positive-ion mode. The ion-source voltage was 4500 V. Nitrogen was used as the nebulizing (20 psi) and curtain (10 psi) gases. The samples were directly infused into the mass spectrometer at a flow rate of 180 $\mu$L/h. The scan range was from $m/z$ 100 to 1500. The simulated spectra were calculated using the *Mmass* software.[27]

Potentiometric studies of **1** were carried out in an $CH_3CN/H_2O$ (1:1, v/v) mixture with a Metrohm 848 Titrino Plus research pH meter fitted with blue-glass and Ag/AgCl reference electrodes, calibrated to read −log [$H^+$] directly, designated as the pH. Equilibrium measurements were performed in a thermostated cell, purged with argon and containing 50.00 mL of the $CH_3CN/H_2O$ (1:1) solution and 0.03 mmol of the complex.[28] The temperature was maintained at 25.00 ± 0.05 °C, and the ionic strength of 0.100 M was maintained constant through the addition of KCl. Computations of the results were carried out with the *BEST7* program, and species diagrams were obtained with the *SPE* and *SPEPLOT* programs.[29]

**Synthesis of Ligands and Complexes.** The ligands $H_2$L and $H_2$L1 were obtained as described elsewhere.[1,21]

*Synthesis of (4-Aminobutyl)pyren-1-ylmethylamine (Pyr-Dab).* In a 250 mL round-bottom flask, 1.25 g (14.0 mmol) of 1,4-diaminobutane was added to 80 mL of methanol. In the next step, 0.46 g (2.0 mmol) of 1-pyrenecarboxaldehyde was added, and the reaction mixture was allowed to react for 6 h at room temperature. The temperature was lowered to 0 °C in an ice bath, 0.08 g (2.0 mmol) of sodium borohydride was added, and the mixture was stirred for 3 h. The pH was adjusted to 5.0, and the solvent was removed under reduced pressure. The resulting solid was dissolved in dichloromethane (DCM) and washed three times with a saturated sodium bicarbonate solution and two times with $H_2O$, resulting in a light-yellow foam (yield: 74%).

IR (KBr pellets, $cm^{-1}$): $\nu$(N−H) 3367, 3290, $\nu$(C−$H_{Ar}$) 3043, $\nu$(C−$H_{Aliph}$) 2934, 2810, $\nu$(C═C) 1594, $\nu$($CH_2$) 1443, $\delta$(C−$H_{Ar}$) 843, 801, $\delta$(C−$H_{Ar}$) 708. $^1$H NMR ($CDCl_3$): $\delta$ −1.53 (4 H, m), 2.73 (4 H, m), 4.46 (2 H, s), 5.76 (1 H, s), 8.05 (8 H, m), 8.35 (1 H, d).

*Synthesis of tert-Butyl-N-{4-[bis(pyren-1-ylmethyl)amino]butyl}-carbamate (Pyr2-Dab-Boc).* In a 125 mL round-bottom flask containing 0.56 g (3.0 mmol) of *N*-Boc-1,4-diaminebutane dissolved in dry tetrahydrofuran (THF), 1.77 g (6.0 mmol) of 1-bromopyrene was slowly added under an argon atmosphere, followed by 1 mL of triethylamine. The mixture was stirred for 12 h under a saturated argon atmosphere. The formation of triethylammonium bromide salt was observed, which was removed by filtration. The filtrate was placed in a rotary evaporator to give a yellowish solid. The solid was then solubilized in DCM and washed with small portions of $NaHCO_3$ (3 × 20 mL) and brine (2 × 20 mL). The organic layer was dried with anhydrous $Na_2SO_4$,


DOI: 10.1021/acs.inorgchem.7b02384
*Inorg. Chem.* XXXX, XXX, XXX−XXX

and the solvent was removed by rotary evaporation, resulting again in a light-yellow foam (yield: 74%).

IR (KBr pellets, $cm^{-1}$): $\nu$(N−H) 3430, $\nu$(C−$H_{Ar}$) 3043, $\nu$(C−$H_{Aliph}$) 2922−2794, $\nu$(C═O) 1697, $\nu$(C═C) 1505, $\nu$($CH_2$) 1362, $\delta$(C−$H_{Ar}$) 843, $\delta$(C−$H_{Ar}$) 708. $^1$H NMR ($CDCl_3$): $\delta$ −1.39 (9 H, s), 1.46 (2 H, m), 1.68 (2 H, t), 2.61 (2 H, t), 2.86 (2 H, m), 4.31 (4 H, s), 8.05 (16 H, m), 8.34 (2 H, d).

*Synthesis of N,N-Bis(pyren-1-ylmethyl)-1,4-butanediamine (Pyr2-Dab).* In a 125 mL round-bottom flask, 1.24 g (2.0 mmol) of Pyr2-Dab-Boc was dissolved in DCM. The system was cooled to 0 °C in an ice bath, and 2.0 mL (ca. 1 mL/mmol) of trifluoroacetic acid was slowly added (the solution acquired a greenish color). The mixture was stirred at room temperature for another 3 h. The organic layer was washed (4 × 20 mL) with an aqueous 2.0 M sodium hydroxide (NaOH) solution and then dried with anhydrous $Na_2SO_4$. The solvent was then removed by rotary evaporation (yield: 82%).

IR (KBr pellets, $cm^{-1}$): $\nu$(N−H) 3423, 3360, $\nu$(C−$H_{Ar}$) 3035, $\nu$(C−$H_{Aliph}$) 2928, 2798, $\nu$(C═C) 1590, $\nu$($CH_2$) 1366, $\delta$(C−$H_{Ar}$) 838, $\delta$(C−$H_{Ar}$) 708. $^1$H NMR ($CDCl_3$): $\delta$ −1.03 (2 H, m), 1.12 (1 H, s), 1.39 (2 H, m), 2.39 (2 H, t), 2.61 (2 H, t), 4.32 (4 H, s), 7.99 (16 H, m), 8.37 (2 H, d).

*Synthesis of $H_2$LP1.* In a 125 mL round-bottom flask, 1.32 g (2.20 mmol) of $H_2$L1 was dissolved in 40 mL of methanol/THF (1:1). In the next step, 30 mL of a THF solution containing 0.66 g of Pyr-Dab (2.20 mmol) was added slowly. The mixture was stirred at room temperature for 3 h. Subsequently, the mixture was cooled to 0 °C in an ice bath, and small portions of $NaBH_4$ were added directly (0.08 g, 2.20 mmol) under constant stirring. The solution was stirred for another 3 h, during which its yellow color gradually faded. A 1.0 M HCl solution was then added in small portions to adjust the pH to 6, and the solvent was removed by rotary evaporation. To the resultant oil was added 80 mL of DCM, and the solution was washed with a saturated aqueous solution of $NaHCO_3$ (3 × 20 mL). The organic layer was dried with solid anhydrous $Na_2SO_4$, and the solvent was removed under reduced pressure. As a result, 1.48 g of a light-yellow foam was obtained (yield: 77%).

IR (KBr pellets, $cm^{-1}$): $\nu$(O−H) 3430, $\nu$(N−H) 3186, $\nu$(C−$H_{Ar}$) 3043, 3007, $\nu$(C−$H_{Aliph}$) 2922, 2810, $\nu$(C═C) 1586, $\nu$(C═N) 1568, $\delta$(O−H) 1365, $\delta$(C−$H_{Ar}$) 843, $\delta$(C−$H_{Ar}$) 768. $^1$H NMR ($CDCl_3$): $\delta$ −1.52 (4 H, m), 2.16 (6 H, s), 2.63 (2 H, m), 2.75 (2 H, m), 3.66−3.80 (14 H, s), 4.43 (2 H, s), 6.76 (4 H, q), 7.09 (3 H, m), 7.34 (3 H, d), 7.55 (3 H, t), 8.03 (8 H, m), 8.29 (1 H, d), 8.50 (3 H, d).

*Synthesis of $H_2$LP2.* In a 125 mL round-bottom flask, 1.17 g (2.0 mmol) of $H_2$L1 was added to 30 mL of a methanol/THF (1:1) mixture. Next, 30 mL of a THF solution, containing 1.03 g of Pyr2-Dab (2.0 mmol), was slowly added. The reaction mixture was stirred at room temperature for 2 h and then cooled to 0 °C in an ice bath. Small portions of $NaBH_4$ were then added directly (0.07 g, 2.0 mmol), and the mixture was stirred for another 1 h. Subsequently, HCI was added in small portions to adjust the pH to 6, and the solvent was removed by rotary evaporation. To the resulting oil was added 60 mL of DCM, and the solution was washed with a 1 M HCl solution (2 × 20 mL), $NaHCO_3$ (3 × 20 mL), and finally $H_2O$ (1 × 20 mL). The organic layer was dried with anhydrous $Na_2SO_4$, and the solvent was removed under reduced pressure. As a result, 1.52 g of a light-yellow foam was obtained (yield: 69%).

IR (KBr pellets, $cm^{-1}$): $\nu$(O−H) 3423, $\nu$(C−$H_{Ar}$) 3041, 3004, $\nu$(C−$H_{Aliph}$) 2919, 2804, $\nu$(C═C) 1591, $\nu$(C═N) 1569, $\nu$(C═C) 1472, $\delta$(O−H) 1362, $\delta$(C−$H_{Ar}$) 843, $\delta$(C−$H_{Ar}$) 754, $\delta$(C═$C_{Ar}$) 708. $^1$H NMR ($CDCl_3$): $\delta$ −1.32 (2 H, q), 1.68 (2 H, q), 2.17 (6 H, s), 2.22 (2 H, m), 2.58 (2 H, m), 3.44 (2 H, s), 3.69−3.82 (12 H, s), 4.29 (4 H, s), 6.84 (4 H, q), 7.07 (3 H, m), 7.37 (3 H, d), 7.51 (3 H, q), 7.82−8.11 (16 H, m), 8.35 (2 H, d), 8.53 (3 H, d).

*Synthesis of [$Fe^{III}Zn^{II}$(LP1)($\mu$-OH)($H_2O$)]($ClO_4$)$_2$ (**1**).* In a 125 mL round-bottom flask, containing 60 mL of a THF/$CH_3CN$ (1:1) solution, the ligand $H_2$LP1 (0.48 g, 0.55 mmol) and $Zn(ClO_4)_2{\cdot}6H_2O$ (0.20 g, 0.55 mmol) were added under stirring at room temperature. To this mixture were added dropwise $Fe(ClO_4)_3{\cdot}9H_2O$ (0.28 g, 0.55 mmol) in 60 mL of $CH_3CN$ and 3 mmol of NaOH in 1.5 mL of $H_2O$. The mixture was stirred for approximately 30 min, and sodium perchlorate ($NaClO_4$; 0.13 g, 1.1 mmol) was then added. The solution was filtered and left to stand. The resulting purple solid was collected and washed with isopropyl alcohol and diethyl ether (yield: 0.36 g, 53%).

Anal. Calcd for $FeZnC_{62}H_{74}N_7Cl_4O_{15}$: C, 52.43; H, 5.25; N, 6.90. Found: C, 52.58; H, 5.26; N, 6.91. IR (KBr pellets, $cm^{-1}$): $\nu$(O−H) 3437, $\nu$(C−$H_{Ar}$) 3037, $\nu$(C−$H_{Aliph}$) 2922, 2861, $\nu$(C═C) 1607, $\nu$(C═N) 1571, $\nu$(C═C) 1470, $\nu$(Cl−O) 1090, $\delta$(C−$H_{Ar}$) 843, $\delta$(C−$H_{Ar}$) 758, $\delta$(C═$C_{Ar}$) 622.

*Synthesis of [$Fe^{III}Zn^{II}$(LP2)($\mu$-OH)($H_2O$)]($ClO_4$)$_2$ (**2**).* Complex **2** was prepared similarly to complex **1** but using $H_2$LP2 instead of $H_2$LP1 as the ligand and as solvents a mixture (1:1) of methanol and chloroform (yield: 0.40 g, 56%).

Anal. Calcd for $FeZnC_{75}H_{79}N_7Cl_5O_{16}$: C, 55.15; H, 4.88; N, 6.00. Found: C, 55.03; H, 4.91; N, 5.95. IR (KBr pellets, $cm^{-1}$): $\nu$(O−H) 3443, $\nu$(C−$H_{Ar}$) 3043, $\nu$(C−$H_{Aliph}$) 2919, 2857, $\nu$(C═C) 1610, $\nu$(C═C) 1474, $\nu$(Cl−O) 1112, 1090, $\delta$(C−$H_{Ar}$) 847, $\delta$(C−$H_{Ar}$) 762, $\delta$(C═$C_{Ar}$) 620.

*Synthesis of [$Fe^{III}Zn^{II}$(L1)($\mu$-OH)($H_2O$)]($ClO_4$)$_2$ (**3**).* This complex was prepared following procedures described in the literature. Anal. Calcd for $FeZnC_{36}H_{40}C_{l2}N_5O_{14}$: C, 45.09; H, 4.20; N, 7.30. Found: C, 44.85; H, 4.14; N, 7.25.

Crystallographic data for **3** were previously deposited.[1]

**Reactivity Measurements.** The phosphodiesterase-like activity was determined for complexes **1** and **2** by monitoring hydrolysis of the substrate BDNPP with a UV−vis Varian Cary 50 BIO spectrometer at 400 nm in an $CH_3CN/H_2O$ (2:1, v/v) mixture due to the low solubility of **2**. The initial rates were measured in real time at various pH values between 4.5 and 10.0 [the buffers used were 0.05 M 2-(*N*-morpholino)ethanesulfonic acid (MES), 2-[4-(2-hydroxyethyl)-piperazin-1-yl]ethanesulfonic acid (HEPES), and *N*-cyclohexyl-2-aminoethanesulfonic acid (CHES)], and the relevant molar absorption coefficients of the reaction product 2,4-dinitrophenolate were determined at each pH under the same experimental conditions as those of the rate measurements.[20] Reactions were monitored to less than 5% depletion of the substrate. The kinetic parameters $k_{cat}$ and $K_M$ were derived using the initial rate methods in a series of buffers ranging from pH 4.5 to 10.0. The pH dependence of the rate (from 4 to 9) was investigated using a substate concentration range of 0.5−6.5 mM and complexes ($[C]_{final}$ = 50.0 $\mu$M for complexes **1** and **2**) at 25 °C ($I$ = 0.05 M with $LiClO_4$). Isotopic effects on the hydrolysis rate of BDNPP promoted by complexes **1** and **2** (i.e., $k_H/k_D$) were investigated by monitoring reactions in deuterated buffers.[21]

**X-ray Crystallography and X-ray Absorption Fine Structure (EXAFS) Analysis.** The structure of $Fe^{III}Zn^{II}$L1 (**3**) has been previously determined by X-ray crystallography.[1] No crystals for **1** and **2** were obtained. In order to compare the effect of the modifications of ligand L1 on the catalytic dinuclear $Fe^{III}Zn^{II}$ center, Fe and Zn K-edge EXAFS data were measured for **1** and **3** in fluorescence mode in 2 mM $CH_3CN$ solutions. Data were collected at the National Synchrotron Light Source, Beamline X3B. Data collection, reduction, and analysis followed published procedures, using *EXAFSPAK*[30] to process the data, which were then fitted in *SIXPACK*, using the calibrated phase and amplitude functions obtained from *FEFF 8.0*.[31] Briefly, for each data set, the Fourier-filtered first shell was fitted while allowing only the absorber−scatterer distance and Debye−Waller factor to vary and stepping through reasonable coordination numbers. The best-fit coordination number was then held fixed in subsequent fits that included outer-shell scatterers.[32]

**Isothermal Titration Calorimetry (ITC).** The binding interactions between complexes **1** and **2** and calf-thymus DNA (CT-DNA) were studied in a 30 mM HEPES buffer at pH 7.0 and 25 °C using a VP-ITC titration calorimeter (MicroCal, Northampton, MA). All solutions were thoroughly degassed before use by stirring under vacuum. The sample cell was loaded with 1.43 mL of a 120 $\mu$M CT-DNA solution, and titration was carried out using a 250 $\mu$L syringe filled with a 500 $\mu$M complex solution, with stirring at 286 rpm. Injections were started after baseline stability had been achieved. A titration experiment consisted of 40 consecutive 6 $\mu$L injections. Each injection lasted 12 s, with a 5 min interval between injections. The values for the heat of dilution of the complex were determined by injecting the complex solution into the buffer alone, and the total observed values for the heat of binding were


DOI: 10.1021/acs.inorgchem.7b02384
*Inorg. Chem.* XXXX, XXX, XXX−XXX

corrected accordingly. The heat released by the dilution of CT-DNA was negligible. At least three titration experiments were performed for each sample set to evaluate the reproducibility. The resulting data were fitted to a single set of identical site models using *ORIGIN* software supplied with the instrument, and the apparent enthalpy change for the binding, $\Delta H$, the binding constant, $K_B$, and the binding stoichiometry, $n$, were obtained. The relative Gibbs free energy change, $\Delta G$, and entropy change, $\Delta S$, for the binding reaction were calculated from the fundamental equations of thermodynamics[33,34]

$$\Delta G = -RT \ln K_a \quad (1)$$

$$\Delta S = \frac{\Delta H - \Delta G}{T} \quad (2)$$

where $K_B$ is the affinity or binding constant ($K_B = 1/K_D$, the dissociation constant), $R$ is the ideal gas constant, and $T$ is the temperature (in Kelvin). In all experiments, the $c$ value ($c = K_B[\text{CT-DNA}]$)[33] was in a range that provides data suitable for the accurate determination of binding constants ($c$ ranged from 76 to 10).[35,36] The reaction heat of the interactions between the complex and DNA is composed of several contributions, which is the reason why the enthalpy must be carefully interpreted as an apparent or observed quantity. It includes not only the effects of the equilibrium between DNA and the complex but also additional equilibria, including solvent effects.[36−38] Nonetheless, it is assumed that the quantity of heat absorbed or released is directly proportional to the extent of binding.

**Determination of the DNA Binding Constant from the Electronic Spectrum.** The intrinsic binding constant $K_b$ was determined from spectral titration data using eq 3:

$$\frac{C_{DNA}}{\varepsilon_a - \varepsilon_f} = \frac{C_{DNA}}{\varepsilon_b - \varepsilon_f} + \frac{1}{K_b(\varepsilon_b - \varepsilon_f)} \quad (3)$$

where $C_{DNA}$ is the concentration of DNA in base pairs and the apparent absorption coefficients $\varepsilon_a$, $\varepsilon_f$, and $\varepsilon_b$ correspond to $A_{obsd}/[M]$, the extinction coefficient of the free compounds. In plots of $C_{DNA}/(\varepsilon_a - \varepsilon_f)$ versus $C_{DNA}$, $K_b$ is given by the ratio of the slope to the intercept. Absorption titration experiments were performed with fixed concentrations of the complexes. Here the complexes were dissolved in a solvent mixture of 25% $CH_3CN$ and 75% HEPES buffer (5 mM HEPES and 50 mM $NaClO_4$, pH 7.0) to avoid the precipitation of DNA. The absorption titration experiments were performed in the absence of and with increasing concentrations of CT-DNA. To obtain the absorption spectra, an appropriate amount of CT-DNA was added to both the compound solution and the reference solution to eliminate the absorbance of CT-DNA itself.

**Plasmid DNA Cleavage.** The DNA cleavage activity of the complexes was evaluated by analyzing conversion of the intact supercoiled form of pBSK II DNA (F I) to open circular (F II) and linear (F III) forms, which represent the plasmid forms containing single- and double-stranded breaks, respectively.[39] Typical reactions were conducted in a final volume of 20 $\mu$L using 330 ng of pBSK II DNA (~25 $\mu$M base pairs) in a 10 mM buffer (MES, HEPES, or CHES, depending on the pH range).[7,40] The cleavage reaction was initiated by the addition of the complexes and incubation for up to 16 h at 37 °C. Each reaction was quenched by adding 5 $\mu$L of a loading buffer solution [50 mM Tris-HCl, pH 7.5, 0.01% bromophenol blue, 50% glycerol, and 250 mM ethylenediaminetetraacetic acid (EDTA)] and then subjected to electrophoresis on a 1.0% agarose gel containing 0.3 $\mu$g/mL ethidium bromide in 0.5 times TBE buffer (44.5 mM Tris, 44.5 mM boric acid, and 1 mM EDTA at pH 8.0) at 90 V for 90 min. The resulting gels were visualized and digitized using a DigiDoc-It gel documentation system (UVP, Upland, CA). The proportion of plasmid DNA in each band was quantified using Kodak Molecular Imaging Software 5.0 (Carestream Health, Rochester, NY). The quantification of supercoiled DNA (F I) was corrected by a factor of 1.47 because the ability of ethidium bromide to intercalate into this topoisomeric DNA form is lower compared with that of open circular and linear DNA.[41] To determine the mechanism by which the complexes perform DNA cleavage, external agents were added to the reaction mixtures. In order to investigate the contribution of electrostatic interactions in the reaction, assays were conducted as described above but with increases in the ionic strength of the reaction medium obtained through the addition of sodium chloride (NaCl; ranging from 50 to 500 mM). Also, different reactive oxygen species (ROS) scavengers,[7] including dimethyl sulfoxide (10%), KI (0.5 mM), superoxide dismutase (20 units), and $NaN_3$ (0.5 mM), were added to the reaction mixture prior to the complex. Assays in the presence of the DNA minor groove binder, netropsin[42] (50 $\mu$M), or the DNA major groove binder, methyl green (50 $\mu$M), were also performed to clarify the DNA groove binding preference of the complexes. The plasmid DNA was pretreated with netropsin or methyl green for 30 min and then treated with the complexes as described above.

In addition, the kinetics of plasmid DNA cleavage performed by **1** and **2** was evaluated following the loss of the supercoiled DNA fraction over time under pseudo-first-order conditions.[43] The apparent plasmid DNA cleavage rates ($k_{obs}$) were obtained from the plot of ln [supercoiled DNA (%)] versus time.

**Cell Lines and Cell Culture.** K562 cells, from a human chronic myelogenous leukemia cell line (CR083; RJCB, Rio de Janeiro, Brazil), were cultured in a RPMI 1640 (Sigma-Aldrich, St. Louis, MO) medium supplemented with 10% fetal calf serum (CULTILAB, São Paulo, Brazil) at 37 °C in a humidified 5% carbon dioxide atmosphere.

SKHep-1 cells, from a human liver cancer cell line (ATCC, Manassas, VA), were cultured at 37 °C in 5% carbon dioxide in Dulbecco's modified Eagle's medium (Invitrogen, Carlsbad, CA) containing 10% fetal bovine serum, 1 mM sodium pyruvate, 50 units/mL of penicillin, and 50 g/mL streptomycin (Invitrogen, Carlsbad, CA).

**Cell Viability Assay.** The cytotoxic effect of the complexes was studied by incubating K562 cells in the absence and presence of different complex concentrations for 24 h. The cells were then counted, and the concentration required to inhibit 50% of cellular growth, $IC_{50}$, was determined. The cell viability was checked by Trypan Blue exclusion. The cell number was determined by Coulter counteranalysis.

**Assessment of Apoptosis.** The quantification of apoptotic cells was performed by flow cytometry using the Alexa Fluor 488 Annexin V/Dead Cell Apoptosis Kit (Thermo Fisher Scientific, Waltham, MA). K562 cells ($1 \times 10^5$ M) were cultured for 24 h in the absence and presence of a range of concentrations of complexes **1** and **3**. The cells were then washed twice with cold phosphate-buffered saline and stained with Alexa Fluor 488 Annexin V and propidium iodide for 15 min at 37 °C in the dark, according to the manufacturer's instructions. Cells were subsequently analyzed with a Guava Easy Cyte 6-2L flow cytometer (Millipore, Burlington, MA). The Alexa Fluor 488 Annexin V and propidium iodide fluorescence data were collected using 525/30 and 583/26 emission filters, respectively. Prior to data collection, the fluorescence signals were compensated for using cells stained with each one of the probes separately. All data were analyzed using *FlowJo* Software (Tree Star, Ashland, OR). Cisplatin at 10 $\mu$M was used as a positive control for apoptosis and late necrosis.

**Fluorescence Microscopy.** *Nuclear Staining.* SKHep-1 cells were detached and incubated ($1 \times 10^5$ cells/well) with 25 $\mu$M complex **1** and 0.5 $\mu$g/mL propidium iodide for 24 h. Representative cells were then selected and photographed. Images were captured using an Olympus IX70 microscope coupled with an Olympus UPlanSApo 60× (NA = 1.35) objective (Olympus, JAP), a Lumen 200PRO illumination source (Prior Scientific Inc., Rockland, MA), and a cooled QIclick camera (Q Imaging, Surrey, British Columbia, Canada). The emission and excitation filters respectively used to collect the fluorescence data for the metal complexes were AT350/50 and AT455/50, and for propidium iodide, they were ET555/25 and ET605/52. The filters and components were controlled by ImagePro (Media Cybernetics, Rockville, MD). Unstained cells were employed as a negative control, and cells stained only with one fluorochrome were employed to compensate for the propidium iodide channel.

*Lysosome Staining.* SKHep-1 cells were detached and incubated ($1 \times 10^5$ cells/well) with 80 $\mu$M complex **1** and 50 nM Lysotracker Red DND-99 for 5 h. Images were captured using a Zeiss 5 Live confocal (Carl Zeiss, Jena, Germany) microscope with a 63× (NA = 1.4) objective lens. The samples were excited at $\lambda_{ex} = 405$ nm and observed at $\lambda_{em} = 425$ nm to detect complex **1** and at $\lambda_{ex} = 543$ nm and $\lambda_{em} = 565-615$ nm to detect Lysotracker.



DOI: 10.1021/acs.inorgchem.7b02384
*Inorg. Chem.* XXXX, XXX, XXX−XXX

## RESULTS AND DISCUSSION

**Synthesis and Characterization of the Ligands and Complexes.** *Synthesis.* The unsymmetrical ligand $H_2L1$, containing a carbonyl moiety attached to the terminal phenol group, was synthesized as described previously.[1] The ligands containing the intercalator pyrene ($H_2LP1$ and $H_2LP2$) were obtained following the synthetic routes described in Schemes S1 and S2, respectively, and were fully characterized through $^1H$ NMR and ESI-MS (Figures S1–S4). The conjugate mixed-valence complexes FeZnLP1 (**1**) and FeZnLP2 (**2**) were synthesized by employing the method described for FeZnL1 (**3**), but using a mixture of $CH_3CN$/THF (1:1) instead of $CH_3OH$ because of the decreased solubility of the ligands.

*Solid-State Structure of 3.* The molecular structure of **3** (Figure 2 and Table 1) shows that in the dinuclear [$Fe^{III}(\mu$-OH)$Zn^{II}$(L1)] unit the coordination/arrangement of L1 and all metric parameters around the metal centers are similar to those observed in the isostructural complex containing ligand $H_2L$.[21]

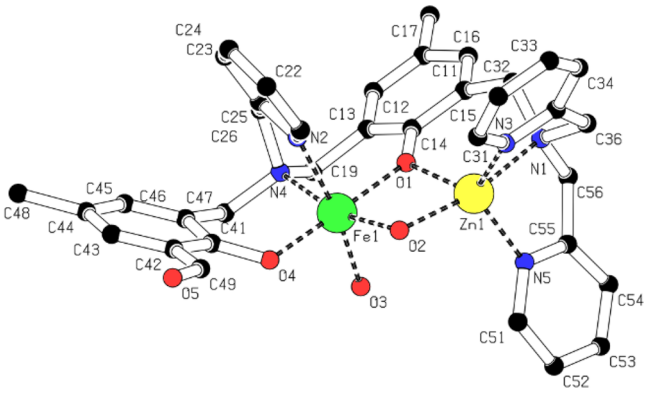


**Figure 2.** ORTEP representation of complex **3**.

**Table 1. Main Bond Distances (Å) and Angles (deg) for the $Fe^{III}Zn^{II}$L1 Complex (3)**[1]

| | | | |
|---|---|---|---|
| Fe1–Zn1 | 3.0550(16) | Fe1–N4 | 2.163(7) |
| Fe1–O2 | 1.912(6) | Zn1–O2 | 1.978(6) |
| Fe1–O4 | 1.925(5) | Zn1–N5 | 2.044(8) |
| Fe1–O1 | 2.032(5) | Zn1–N3 | 2.062(8) |
| Fe1–O3 | 2.082(6) | Zn1–O1 | 2.079(5) |
| Fe1–N2 | 2.132(7) | Zn1–N1 | 2.149(6) |
| | | | |
| O2–Fe1–O4 | 101.2(3) | O1–Fe1–O3 | 90.4(2) |
| O2–Fe1–O1 | 81.1(2) | O2–Fe1–N2 | 96.8(3) |
| O4–Fe1–O1 | 177.7(3) | O4–Fe1–N2 | 86.2(3) |
| O2–Fe1–O3 | 93.5(3) | O1–Fe1–N2 | 93.9(2) |
| O4–Fe1–O3 | 89.2(2) | O3–Fe1–N2 | 169.4(3) |

Briefly, in the dinuclear complex, the iron(III) center is facially coordinated by the hard tridentate pendant arm of the L1 ligand containing an amine (N4) and a pyridine (N2) nitrogen atoms and a phenolate oxygen (O4) atom, while zinc(II) is coordinated by the soft side of the ligand through an amine (N1) and two pyridine (N3 and N5) nitrogen atoms. The bridging phenolate oxygen (O1) atom, the bridging hydroxo group (O2), and a terminal $H_2O$ molecule (O3) complete the pseudooctahedral $N_2O_4$ coordination of iron(III), while the distorted trigonal bipyramid of zinc(II) ($\tau = 0.67$) is complemented by the bridging phenolate (O1) and hydroxo (O2) oxygen atoms. The Fe···Zn distance is 3.0550(16) Å in $Fe^{III}Zn^{II}$L1 and 3.040(1) Å in the $Fe^{III}Zn^{II}$L complex. This internuclear distance is in good agreement with the EXAFS measurements of **1**, which indicated that the two metal ions are separated by ~3.00 Å (Table 2). It is important to note that in addition to the terminal iron-bound $H_2O$ molecule [Fe···O3 = 2.082(6) Å], which has been proposed as the nucleophile in the hydrolysis of diesters catalyzed by [$Fe^{III}(\mu$-OH)$Zn^{II}$(L)],[21] the structure of **3** contains a carbonyl group (i.e., C···O5) located in the ortho position to the terminal iron(III)-bound phenolate ligand. From the solid-state structure of **3** (Figure 2), it is evident that this functional group is ideally oriented for further chemical reactions. Consequently, ligand L1 was modified at this position to contain one ($H_2LP1$) or two ($H_2LP2$) pyrene groups conjugated to the dinucleating ligand by a 1,4-diaminobutane spacer (Chart 1).

**Table 2. EXAFS-Derived Metrical Parameters (Å) for FeZnL1 (3) and FeZnLP1 (1)**[a]

| sample | Fe–N/O | Zn–N/O | Zn–Fe |
|---|---|---|---|
| FeZnL1 (**3**) | 6/1.95 | 5/2.07 | 3.00 |
| FeZnLP1 (**1**) | 6/1.97 | 5/2.11 | 3.00 |

[a]See Figure S5.

*Solution Structures of 1 and 3.* The pyrene groups were expected to be structurally mobile additions to ligand L1. Consequently, it was no surprise that no crystals of the corresponding FeZn complexes could be obtained. Thus, in order to probe whether these ligand modifications affect the geometry of the catalytically relevant [$Fe^{III}(\mu$-OH)$Zn^{II}$] unit, the solution structures of **1** and **3** were studied by EXAFS, at both the Zn and Fe K-edges (Table 2 and Figure 3; detailed information is given in Figure S5).

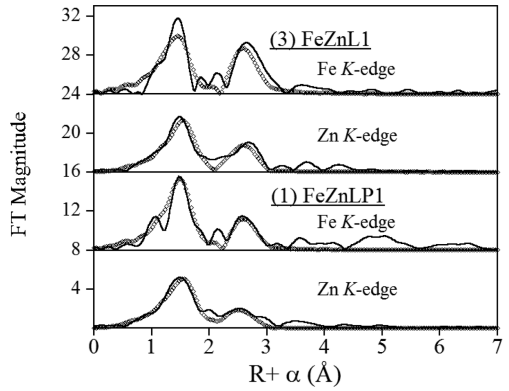


**Figure 3.** EXAFS Fourier transforms (solid lines) and corresponding best fits (for open symbols, see Table 2) for 2 mM $CH_3CN$ solutions of complexes **1** and **3** at the Fe and Zn K-edges.

As can be seen in Figure 3, the iron and zinc EXAFS spectra of the parent complex **3** and the asymmetric complex **1** are very similar in a $CH_3CN$ solution. Each Fourier transform is dominated by the primary donors to the respective metals ($R + \alpha \sim 1.6$ Å) and one significant long-range interaction.

Each data set was fitted with a simple model of one shell of low-$Z$ atoms (N/O) and one long-distance metal–metal (Fe···Zn) scattering interaction. The Zn–N/O distances (2.07 and 2.11 Å) are fully consistent with a five-coordinate zinc(II) ion in a nitrogen-rich environment and are in good agreement with the average obtained by diffraction (2.06 Å). In contrast, the Fe···N/O distances in a $CH_3CN$ solution, while consistent with six-


DOI: 10.1021/acs.inorgchem.7b02384
Inorg. Chem. XXXX, XXX, XXX–XXX

coordinate iron(III) in an oxygen-rich environment, are ~0.08 Å shorter than indicated by the crystal structure. This may reflect a tendency for $CH_3CN$ to facilitate dissociation of the terminal hydroxyl, leaving a six-coordinate iron with one weakly bound solvent. The iron X-ray absorption near-edge structure results support an iron coordination number of 6, with integrated 1s → 3d areas of $9.3 \times 10^{-2}$ eV for both complexes (Figure S5).[44] In addition, and perhaps most importantly, the EXAFS data show that the multiply bridged structure seen in the solid state is retained in solution, with equivalent distances determined from both the Zn and Fe K-edges, for the two complexes.

**Solution Studies (ESI-MS, UV−vis, Electrochemistry, and Potentiometric Titration).** In order to establish the catalytically active species in the hydrolysis of diester bonds, ESI-MS, electronic spectroscopy, electrochemistry, and potentiometric titration studies were carried out in $CH_3CN$ or $CH_3CN/H_2O$ solutions.

ESI-MS analysis of complex **1** was performed in a pure $CH_3CN$ solution (500 nM). A group of peaks with a maximum (100%) at $m/z$ 517.1 with a 2+ charge was observed (Figure S6). This signal can be assigned to the system $[Fe^{II}Zn^{II}(\mu\text{-}OH)(LP1)] + OH_2 + Li^+$, suggesting a reduction in the iron(III) center under the ESI-MS conditions. For the molecular ion of the complex, it is reasonable to assume that two $H_2O$ molecules are terminally coordinated to the metal centers. Adducts formed with some ions, such as $Na^+$, $K^+$, $Li^+$, and $NH_4^+$, commonly occur in mass spectrometry experiments[45] and possibly originate from the glass containers used in the sample preparation or the sample injection line. Complex **2** showed a group of peaks with a maximum (100%) at $m/z$ 649.2 with a 2+ charge. This peak is assigned to the system $[Fe^{III}(\mu\text{-}OH)Zn^{II}(LP2)(OH_2)] + OH_2 + Na^+$, which corresponds to the molecular ion of the complex having a $H_2O$ molecule and a terminal hydroxo ion bound to the metal centers, a hydration $H_2O$, and a sodium ion. Figure S7 shows the mass spectrum for complex **2**.

The UV−vis absorption spectra of complexes **1**−**3** were investigated in the range of 200−900 nm, using $CH_3CN$ or $H_2O/CH_3CN$ (2:1, v/v) as the solvents. In pure $CH_3CN$ solutions, complexes **1** and **2** show strong absorption bands at $\lambda_{max}$, nm ($\varepsilon$, $M^{-1}$ $cm^{-1}$), of 512 (2100) and 510 (2300), respectively (Table 3), assigned to a ligand-to-metal charge-transfer (LMCT) transition from the p$\pi$ orbitals of the phenolate to the d$\pi$* orbitals of the iron(III) ion. Similar transitions are also observed in PAPs.[46] For both complexes (as well as PAPs), a second transition is observed as a shoulder at 330 nm, which is also assigned to a LMCT transition involving the p$\pi$ orbitals of the phenolate and the d$\sigma$* orbitals of the iron(III) center. Relative to **1** and **2**, the lower-energy LMCT transition of **3** is shifted by around 50 to ~560 nm. The electronic properties of a series of $[Fe^{III}(\mu\text{-}OH)Zn^{II}(L)]$ complexes, where the terminal phenolate moiety was modified to contain electron-donating or -withdrawing groups (i.e., $-CH_3$, −H, −Br, $-NO_2$), have been studied in some detail with a variety of experimental and computational techniques.[20] For these complexes, it has been shown that withdrawing groups (−Br, $-NO_2$) tend to shift the (p$\pi$)phenolate → (d$\pi$)$Fe^{III}$ LMCT band to higher-energy values, while a bathochromic shift is observed for the donating $-CH_3$ group compared to −H. According to the $\lambda_{max}$ values of **1** and **2**, a positive charge on the side chain, due to the protonated amino groups (see potentiometric titration), could shift this $\lambda_{max}$ value to higher-energy values, which simulates the effect of a withdrawing group on the aromatic phenolate ring.

**Table 3. Electronic Spectral and Electrochemical Data for Complexes 1−3**

| | $\lambda_{max}$, nm ($\varepsilon$, $M^{-1}$ $cm^{-1}$) | | |
|---|---|---|---|
| complex | $CH_3CN$ | $CH_3CN/H_2O$ (2:1) | $E_{1/2}$ (mV vs NHE) |
| **1** | 512 (2100) | 506 | −189 |
| **2** | 510 (2300) | 491 | −196 |
| **3** | 562 (2080) | | −252 |

The electrochemical behavior of complexes **1** and **2** was studied by cyclic voltammetry in an $CH_3CN/H_2O$ (2:1, v/v) solution (Table 3). For both complexes, the cyclic voltammograms show one *quasi*-reversible redox process, which can be attributed to the $Fe^{III}/Fe^{II}$ redox couple. Typical cyclic voltammograms for the two complexes are shown in Figure S8. The redox potentials of **1** ($E^{1/2}$ = −189 mV) and **2** ($E^{1/2}$ = −196 mV) vs NHE are comparable with those found for the $[Fe^{III}(\mu\text{-}OH)Zn^{II}(L\text{-}R)]$ complexes (R = $-CH_3$, −H, −Br, $-NO_2$).[1,20] However, the influence of the positive charge on the amino groups in the side chains of the modified ligands led to values that are anodically shifted by around 50 mV compared to the $E_{1/2}$ value of complex **3**. This observation is in full agreement with the UV−vis spectra for the complexes (vide supra), which show that the (p$\pi$)phenolate → (d$\pi$)$Fe^{III}$ LMCT band of **1** and **2** is shifted to lower $\lambda_{max}$ (higher energies) compared to that of **3**.

Equilibrium studies were carried out by the potentiometric titration of complex **1** in an $CH_3CN/H_2O$ (1:1) mixture.[28] The results indicate the neutralization of 4 mol of potassium hydroxide per mole of complex in the pH range 3.00−12.00. The corresponding p$K_a$ values are listed in Table 4, and species distribution graphs are shown in Figure S9. Because of low solubility, complex **2** was studied by spectrophotometric titration in an $CH_3CN/H_2O$ (2:1) mixture, and only p$K_{a1}$ could be determined. Although the experimental conditions used for complexes **1** and **2** were not strictly the same and thus we cannot directly compare the p$K_a$ values, it seems reasonable to correlate the p$K_a$ values among each other.

**Table 4. Values of the Protonation Constants for Complexes 1−3**[a]

| | p$K_{a1}$ | p$K_{a2}$ | p$K_{a3}$ | p$K_{a4}$ |
|---|---|---|---|---|
| **1** | 4.21 ± 0.03 | 6.85 ± 0.02 | 9.09 ± 0.02 | 11.39 ± 0.04 |
| **2** | 4.27 ± 0.08 | | | |
| **3** | 5.07 | 8.21 | | |

[a]The data for **3** have been previously reported.

The first protonation constant (p$K_{a1}$) may be attributed to a $H_2O$ molecule bound to iron(III), while the second constant (p$K_{a2}$) is attributed to deprotonation of the $H_2O$ molecule bound to zinc(II). The third and fourth constants (p$K_{a3}$ and p$K_{a4}$) are assigned to the protonation/deprotonation equilibria of two amines from the 1,4-diaminobutane group in the side chain of complex **1**, an assignment that is in agreement with the values for free amines in solution.[47] The first and second p$K_a$ values of **1** are rather low for terminally coordinated $H_2O$ molecules and are approximately one pH unit lower than the corresponding constants reported for complex **3** (Scheme 1 and Figure S9). This observation may be interpreted in terms of electrostatic interactions between the protonated amino groups in the side chain of the complex and the iron(III)/zinc(II)-coordinated $H_2O$ molecules. A proposal for the protonation equilibria observed for complex **1** is shown in Scheme 1. A similar


DOI: 10.1021/acs.inorgchem.7b02384
Inorg. Chem. XXXX, XXX, XXX−XXX

**Scheme 1. Proposed Equilibrium Species for Complex 1 in a $H_2O/CH_3CN$ (1:1) Solution**

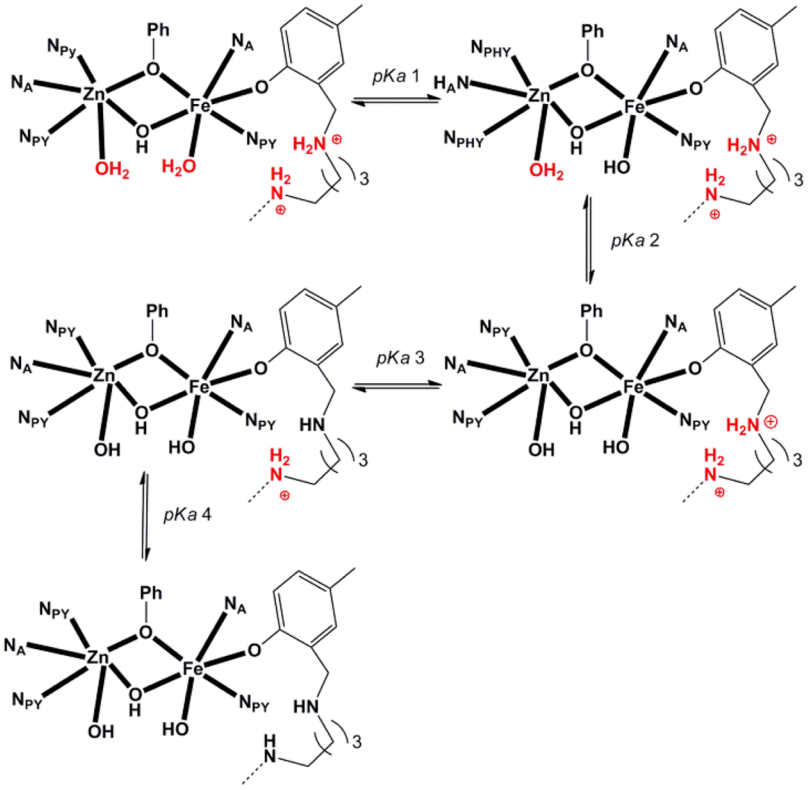


scheme is also likely for complex **2**, although only $pK_{a1}$ could be determined through spectrophotometric titration because of the low solubility of this species (Figure S10).

**Reactivity Studies.** The phosphodiesterase-like activity of complexes **1** and **2** was evaluated in an $CH_3CN/H_2O$ (2:1, v/v) mixture using the activated substrate BDNPP under pseudo-first-order conditions ([S] ≫ [complex]). The reaction was monitored spectrophotometrically at 400 nm, the absorption maximum of the product 2,4-dinitrophenolate.[20] The pH dependence of the catalytic activity for both complexes was obtained with the plot of $k_{cat}/K_M$ (obtained at each pH value) versus pH (Figure 5). At each pH value, the excess of the substrate curve was obtained by using the initial rate method, and it was possible to use the Michaelis−Menten equation $V_0 = V_{max}\{[S]/([S] + K_M)\}$ to calculate the kinetic parameters $k_{cat}$ and $K_M$. The kinetic $pK_a$ values were obtained from sigmoidal fits of the data for each curve at the corresponding adequate pH range. At least two protonation equilibria are relevant to catalysis (Figure 4 and Table 5). The optimal pH for **1** is ~6.5, while **2** reaches its maximum activity at pH ~8.0. While the $pK_a$ values obtained via kinetic and potentiometric titration experiments for **3** are similar, the acid dissociation constants determined for **1** and **2** from kinetic assays, as far as available, are shifted to more alkaline values compared to the values estimated from potentiometric titrations (see Tables 4 and 5).

This observation may suggest that the presence of the BDNPP substrate prevents interaction between the protonated amine side chain of the ligand and the $H_2O$ ligands coordinated to the metal ions. This hypothesis was probed by recording the fluorescence spectra of **1** as a function of the BDNPP added (Figure 5). The emission spectrum of **1** shows a strong band at 460 nm, which is typical for pyrene excimers, most probably due to intermolecular interactions.[48] In general, the broad emission

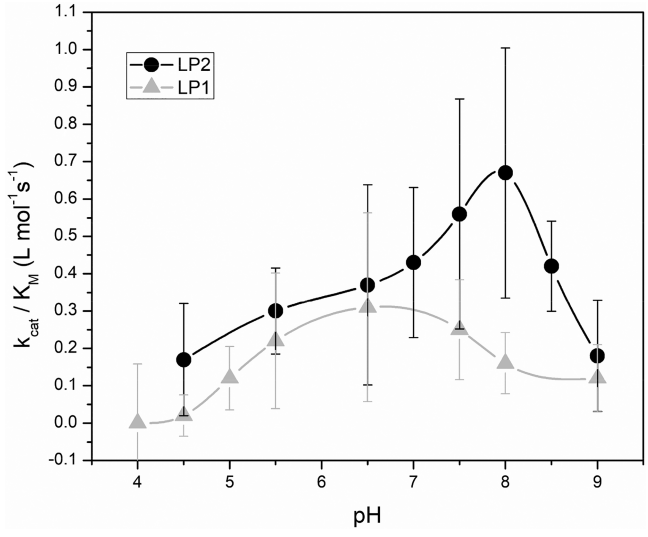


**Figure 4.** Dependence of the catalytic efficiency on the reaction rates at the pH for hydrolysis of BDNPP by **1** (●) and **2** (gray-shaded ▲).

**Table 5. Comparison of Values for the Potentiometric and Kinetic $pK_a$ for 1−3**[a]

| | potentiometric | | kinetic | |
|---|---|---|---|---|
| | $pK_{a1}$ | $pK_{a2}$ | $pK_{a1}$ | $pK_{a2}$ |
| **1** | 4.21 ± 0.03 | 6.85 ± 0.02 | 5.34 ± 0.14 | 7.54 ± 0.11 |
| **2** | 4.27 ± 0.08 | | 5.49 ± 0.10 | |
| **3** | 5.07 | 8.21 | 4.90 | 7.90 |

[a]The data for **3** have been previously reported.

centered at 460−480 nm is extremely easy to recognize as the result of the excimer of pyrene derivatives because monomer



DOI: 10.1021/acs.inorgchem.7b02384
Inorg. Chem. XXXX, XXX, XXX−XXX

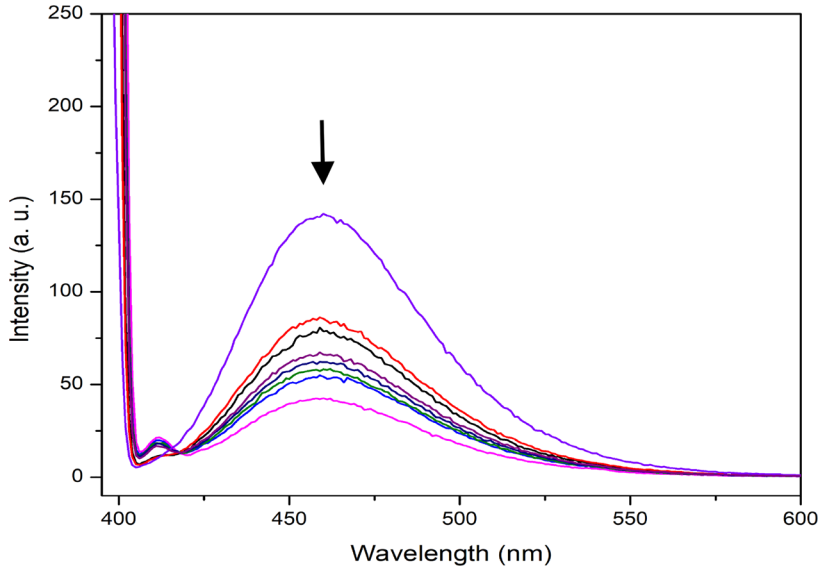


**Figure 5.** Quenching of the fluorescence of complex **1** by successive additions of BDNPP.

fluorescence takes place in the 380−420 nm wavelength range. As can be seen in Figure 5, upon binding of the substrate, the emission of the pyrene excimer decreases while the fluorescence of the monomer slightly increases, suggesting that the substrate binds to the active site in the vicinity of the pyrene group, thus affecting the fluorescence properties of this group but possibly also the interactions of the protonated amino groups with the metal-bound $H_2O/OH^-$.

Similar to the assignments described in the potentiometric titration analysis (see above), $pK_{a1}$ = 5.34 obtained from the kinetic data for **1** may be attributed to the deprotonation of the terminal iron(III)-bound $H_2O$ molecule and the formation of the active species $[(OH)Fe^{III}(\mu\text{-}OH)Zn^{II}(OH_2)]$, while $pK_{a2}$ is assigned to deprotonation of the $H_2O$ molecule bound to zinc(II).[20] The increase in $k_{cat}$ between pH 4.5 and 7.0 is due to formation of the nucleophile, while the decrease between pH 7.5 and 8.5 is interpreted in terms of a reduced association (characterized by $K_{ass}$) of the substrate [a deprotonated zinc(II)-bound $H_2O$ molecule may interfere with the effective substrate binding]. This interpretation is consistent with the mechanism proposed for the related $Fe^{III}Zn^{II}L$ complex.[21] The pH dependence of **2** is more complex and resembles that of some PAPs and related model complexes for which a minimum of three relevant protonation equilibria have been identified. The data were fitted using a Boltzmann model, and a sigmoidal fit of the curves revealed the following $pK_a$ values: $pK_{a1}$ = 5.32; $pK_{a2}$ = 7.41; $pK_{a3}$ = 8.48. The $pK_{a1}$ and $pK_{a3}$ values for **2** are likely to correspond to the $pK_{a1}$ and $pK_{a2}$ values for **1** (Table 5). The assignment of $pK_{a2}$ for **2** remains obscure, but an attractive suggestion invokes a role for the tertiary amine group of ligand LP2 (Chart 1) in substrate binding. In its deprotonated (neutral) form (i.e., above $pK_{a2}$), this residue may promote optimal interactions between the two pyrene moieties of the ligand and the phenol group of the substrate.

The effect of the substrate concentration on the catalytic rate at pH 6.5 reveals Michaelis−Menten-like behavior for **1** and **2**. Relevant kinetic parameters (Figure 6 and Table 6) were obtained by fitting the data to the Michaelis−Menten equation by nonlinear regression.

The kinetic parameters for **2** were also determined at pH 8.0, the optimum pH for this species in hydrolysis of BDNPP. As can be seen from the data in Table 6 that, under these experimental conditions, the substrate binding constant ($K_{ass}$) is only a little lower than that obtained at pH 6.5, while $k_{cat}$ is increased, suggesting that the maximum catalytic efficiency of **2** is attained when the side-chain amine residue becomes deprotonated and promotes optimal interactions with the substrate (vide supra).

The $k_{cat}$ values obtained for **1** and **2** at pH 6.5 are similar, but the value for complex **3** is 3−4 times higher (Table 6). A possible reason for this difference may originate from interaction of the substrate BDNPP with the ligand side chain, thus increasing the

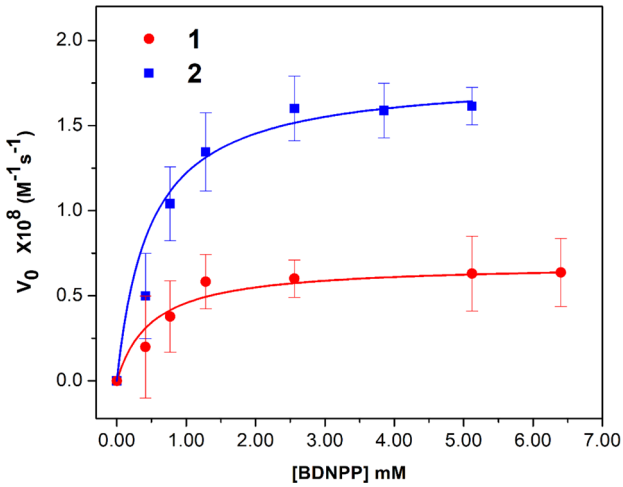


**Figure 6.** Dependence of the reaction rates on the concentration of BDNPP for **1** and **2** at pH 6.5.

**Table 6. Kinetic Parameters of Complexes 1−3 for BDNPP Hydrolysis at pH 6.5**[a]

| | $k_{cat}$, $\times 10^4$ $s^{-1}$ | $K_M$, $\times 10^4$ M | $K_{ass}$, $\times 10^{-3}$ $M^{-1}$ | $k_{cat}/K_M$, $M^{-1}$ $s^{-1}$ |
|---|---|---|---|---|
| **1** | 2.10 ± 0.14 | 6.60 ± 0.34 | 1.5 | 0.32 ± 0.34 |
| **2** | 2.90 ± 0.29 | 5.10 ± 0.18 | 1.9 | 0.56 ± 0.62 |
| **2**[b] | 3.80 ± 0.10 | 5.5 ± 0.11 | 1.8 | 0.67 ± 0.61 |
| **3**[c] | 9.0 | 35.0 | 0.27 | 0.25 |

[a]The data for **3** have been previously reported.[1] [b]At pH 8.0. [c]Reference 1.



DOI: 10.1021/acs.inorgchem.7b02384
*Inorg. Chem.* XXXX, XXX, XXX−XXX

$K_{ass}$ values for **1** and **2** by a factor of ~6 compared to **3**. Nevertheless, despite the improved binding in comparison to **3** (i.e., increased $K_{ass} = 1/K_M$ values), the substrate may not be adequately positioned for a nucleophilic attack by the $Fe^{III}$-OH group in **1** and **2** (Figure 7). A comparison of the catalytic

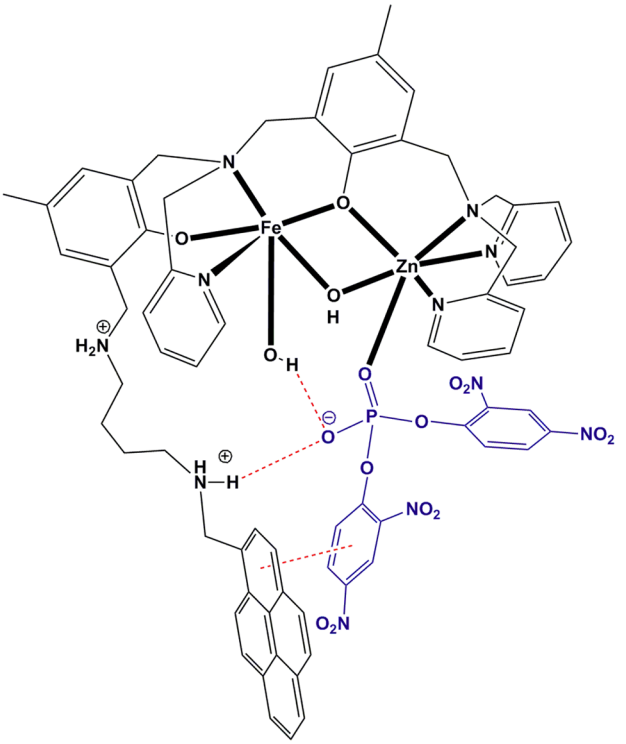


**Figure 7.** Proposal for interactions between the substrate and complex **1**.

efficiencies of **1** and **2** with that reported for a heterovalent $Fe^{III}Fe^{II}$ complex containing a derivative ligand of L1 with $NH_2$ substituents at the pyridyl groups for hydrogen bonding with BDNPP reveals that these parameters are of the same order but again with $K_{ass}$ for **1** and **2** being 6 times higher for complexes containing a lateral chain.[49]

In order to determine whether the complexes also show monoesterase activity, their capability of hydrolyzing DNPP, a product of their diesterase activity, was tested. A stoichiometric reaction (1:1 complex/substrate) was performed at 25 °C for 24 h. As observed for the FeZnL and **3** complexes, only the diesterase activity was observed for both complexes **1** and **2**.[20,21] **1** and **2** showed respectively 10 and 13 turnovers in 24 h at pH 6.5 and 25 °C.

To investigate whether a general base reaction mechanism can be attributed to **1** and **2**, the effect of the deuterium isotope on the hydrolytic cleavage of BDNPP was studied under identical conditions using either $H_2O$ or $D_2O$. The values for $k_H/k_D$ for complexes **1** and **2** were respectively 1.24 and 1.12, indicating that there is no proton transfer in the rate-limiting step of the reaction ($0.80 < k_H/k_D < 1.50$), thus lending support to a mechanism invoking an intramolecular nucleophilic attack by a metal-bound hydroxide to initiate hydrolysis.[50]

**Activation Parameters.** The influence of the temperature on the hydrolysis reaction was investigated for complexes **1**−**3**. The experimental conditions were the same as those described above for the pseudo-first-order experiments, and the temperatures were varied from 25 to 50 °C (Figure S11). A comparison of the activation parameters of the uncatalyzed reaction versus that catalyzed by **3** reveals that the catalyst has only a minor influence on $\Delta S^{\ddagger}$ of the process (similar $T\Delta S^{\ddagger}$ values for the two reactions indicate similar structural organizations of their TSs). Therefore, the effect of **3** on the process is basically enthalpic (Table 7); it favors the reaction ($k_{cat}$) by bond making in the TS.

**Table 7. Activation Parameters Obtained from Eyring Plots**

| | $\Delta H^{\ddagger}$ (kJ mol$^{-1}$) | $T\Delta S^{\ddagger}$ (kJ mol$^{-1}$) | $\Delta G^{\ddagger}$ (kJ mol$^{-1}$) |
|---|---|---|---|
| $H_2O$[a] | 79.0 | −34.4 | 113.8 |
| **1** | 48.6 ± 0.5 | −49.6 ± 0.3 | 98.2 ± 0.6 |
| **2** | 48.7 ± 0.3 | −45.8 ± 0.2 | 94.5 ± 0.4 |
| **3** | 58.5 ± 0.1 | −33.2 ± 0.1 | 91.7 ± 0.2 |

[a]Reference 51.

In contrast, the influence of the protonated 1,4-diaminobutane linker and the pyrene group(s) in complexes **1** and **2** is expected to manifest itself via both enthalpic and entropic effects. The presence of an increased number of hydrogen bonds (secondary effects) is expected to enhance the stability of the TS compared to **3** (Table 7).

However, the favorable contribution of enthalpy changes to the reactivity of **1** and **2** are offset by less favorable changes in $\Delta S^{\ddagger}$ in comparison to **3**. This may be a reflection of an enhanced structural organization in the TS. A similar effect has been observed for reaction of the polyethylenimine-modified complex $FeCuL^1$ with the same substrate (BDNPP), in which the polymer showed an even greater effect on $\Delta S^{\ddagger}$.[7] In summary, these results demonstrate that adequate interactions between the first and second coordination spheres of the catalyst are necessary to achieve higher catalytic activity. It is encouraging to note that the presence of two pyrene groups in **2** reduces the negative impact of $\Delta S^{\ddagger}$, possibly by introducing a degree of asymmetry to the complex/substrate in the TS.

On the basis of the combined structural and kinetic data, the reaction mechanism shown in Scheme 2 is proposed for hydrolysis of the phosphate diester BDNPP by **1**.

First, the substrate binds monodentately to the zinc(II) ion of the $[(OH)Fe^{III}(\mu\text{-}OH)Zn^{II}(OH_2)]$ unit by displacing its labile $H_2O$ ligand. Hydrogen-bonding and electrostatic interactions via the protonated 1,4-diaminobutane linker as well as hydrophobic interactions with the pyrene group(s) significantly increase the $K_{assoc}$ value of the substrate compared to complex **3**. The next step is characterized by the nucleophilic attack of the terminal iron(III)-bound hydroxo group of the bound substrate and the concomitant release of the 2,4-dinitrophenolate leaving group. In this step, hydrogen-bonding formation and stabilization of the negatively charged TS are likely because the $\Delta H^{\ddagger}$ values for **1** and **2** are decreased by ~10 kJ mol$^{-1}$ with respect to that of **3**. Finally, the $\mu$-1,3-coordinated monoester product DNPP is displaced by two $H_2O$ molecules from the environment, and the active site is regenerated. In conclusion, the main difference in the mechanisms associated with **1**−**3** is related to the second-coordination-sphere effects, which lead to tighter substrate binding and a higher degree of structural order in the TSs of **1** and **2**) On the other hand, it is important to mention here that the secondary effects result in a decrease of the catalytic activity ($k_{cat}$) of **1** and **2**, most probably due to the strong electrostatic interaction of BDNPP and the protonated amino group(s), and thus the substrate may not be adequately positioned for a nucleophilic attack by the $Fe^{III}$-OH group.


DOI: 10.1021/acs.inorgchem.7b02384
Inorg. Chem. XXXX, XXX, XXX−XXX

**Scheme 2. Proposed Mechanism for Hydrolysis of Phosphate Diester Promoted by Complex 1**

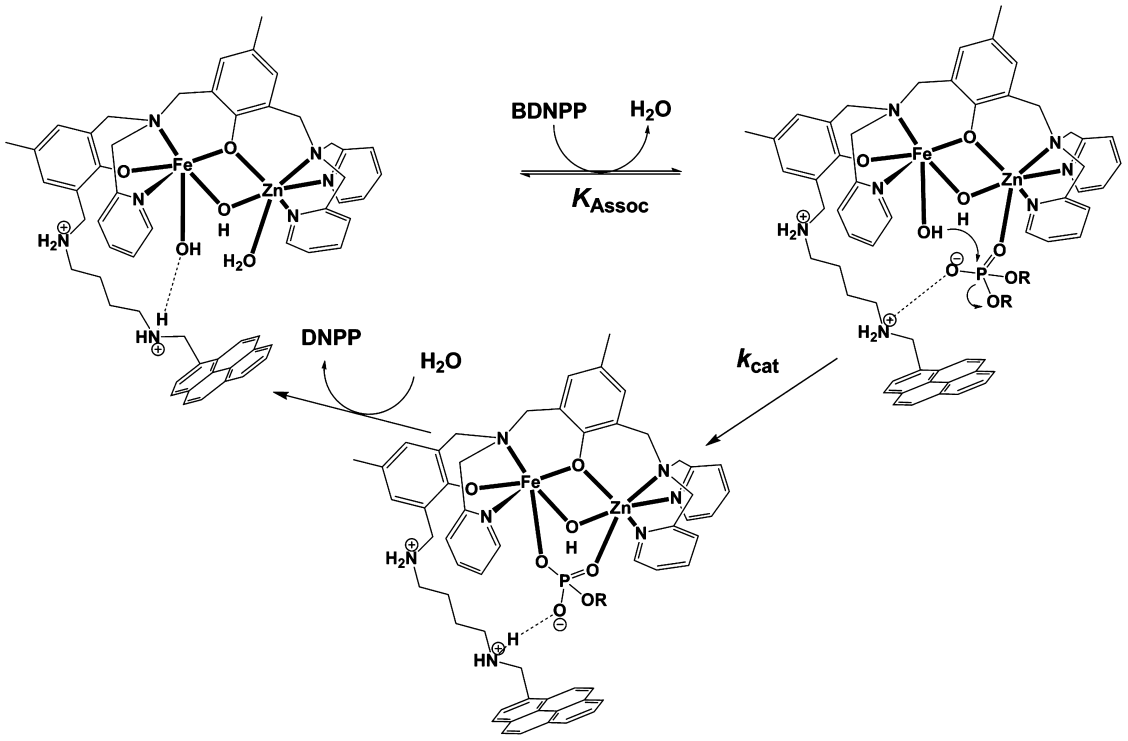


**DNA Binding Studies.** The investigation of the interactions of coordination compounds with DNA via absorption spectroscopy generally results in hypochromism and also a bathochromic shift in the charge-transfer bands.[48,52,53] This is largely due to $\pi$-stacking interactions between aromatic rings from the complex and DNA base pairs. Here, binding of the potentially intercalative complexes **1** and **2** to DNA was initially assessed through titration, by following the changes in the absorbance intensity and wavelength. The pyrene group has a well-known band at around 350 nm related to a $\pi-\pi^*$ transition,[48] which is commonly used in the study of the pyrene group interaction with DNA by spectrophotometric titration. Absorption spectra for complexes **1** and **2** in the presence of CT-DNA are shown in Figures S12 and S13. As the concentration of DNA was increased, the $\pi-\pi^*$ transition bands of the pyrene group exhibited hypochromism, indicating that the complexes bind to CT-DNA through intercalation. On the basis of the decrease in the absorbance values for complexes **1** and **2**, their respective binding affinities (i.e., binding constants $K_b$) for CT-DNA could be determined. The values obtained are reported in Table 8 and Figures S12 and S13.

An experiment using three different oligonucleotides was performed to identify a preference for A−T or C−G base pairs. In a manner similar to that used for CT-DNA, three different oligonucleotides (pAT, 5′-CATATATATA-CCCC- TATATA-TATG-3′; p50AT, 5′-CGCATATGGC-TTTT-GCCA-TATGCG-3′; pGC, 5′-CGCGCGCGCGC-TTTT-GCGCGCGCGCG-3′) were added in small portions to a solution containing complex **1**. The results show similar $K_b$ values for CT-DNA and the oligonucleotide pAT (AT-rich), indicating a probable preference of pyrene-containing complexes for A−T pair regions. For the pGC (GC-rich) oligonucleotide, the $K_b$ constant values were around 25% of these values. Finally, with the last oligonucleotide (p50AT), the constant decreased by around 50%, as expected, because it has 50% of A−T pairs. The binding interactions between the complexes and CT-DNA were further examined by ITC (Table 9). These studies show positive enthalpy terms, based on the endothermic profile of the reactions, with stoichiometries between 2 and 4 base pairs of DNA per complex, that is, similar to those previously reported for related systems.[54,55]

**Table 8. Binding Constants ($K_b$) for the Interaction of CT-DNA, Oligonucleotides, and Complexes 1 and 2**

| | $K_b \times 10^{-5}$ ($M^{-1}$) | $K_b$(pAT) $\times 10^{-5}$ ($M^{-1}$) | $K_b$(pGC) $\times 10^{-4}$ ($M^{-1}$) | $K_b$(p50AT) $\times 10^{-5}$ ($M^{-1}$) |
|---|---|---|---|---|
| **1** | 2.4 ± 0.4 | 2.7 ± 0.2 | 6.8 ± 0.7 | 1.3 ± 0.4 |
| **2** | 12.1 ± 0.3 | | | |

The DNA binding constants of complexes with modified ligands increase significantly (from $1.42 \times 10^5$ to $1.08 \times 10^6$ $M^{-1}$) compared to that of **3**. Interestingly, the presence of two pyrene groups (in **2**) instead of only one (in **1**) increases the affinity by around a factor of 2 (note that the binding constants determined by ITC are in reasonable agreement with those obtained from the spectrometric titrations).

ITC measurements provide insight into the driving force for a particular binding interaction.[56] As shown in Figure 8, the interaction between DNA and **3** is largely driven by favorable entropy changes to overcome the large enthalpic penalty. In contrast, the incorporation of pyrene groups in complexes **1** and **2** leads to nearly enthalpy-neutral interactions with DNA but with considerably smaller contributions from entropy changes compared to **3**. These observations are in agreement with the TS analysis (Table 9) and reinforce the interpretation that the pyrene rings afford an increased structural order of the catalyst/substrate (i.e., DNA) complex.

**Plasmid DNA Cleavage.** Assays were performed to determine the DNA cleavage efficiencies of **1** and **2** as a function of the pH (Figure 9; the spontaneous fragmentation of DNA was



DOI: 10.1021/acs.inorgchem.7b02384
Inorg. Chem. XXXX, XXX, XXX−XXX

**Table 9. Thermodynamic Parameters $K_B$, $\Delta H$, and $n$ Directly Determined by ITC Using the Single Set of Identical Site Models[a]**

| complex | $n$ | $K_B$ ($M^{-1}$) | $\Delta H$ (kJ $mol^{-1}$) | $T\Delta S$ (kJ $mol^{-1}$) | $\Delta G$ (kJ $mol^{-1}$) |
|---|---|---|---|---|---|
| **1** | 2.28 ± 0.02 | (6.3 ± 0.2) × $10^5$ | 5.7 ± 0.1 | 38.8 ± 1.3 | −33.1 ± 0.2 |
| **2** | 3.30 ± 0.02 | (1.1 ± 0.1) × $10^6$ | 3.5 ± 0.1 | 37.8 ± 1.0 | −34.3 ± 0.1 |
| **3** | 3.64 ± 0.01 | (1.4 ± 0.2) × $10^5$ | 38.5 ± 0.3 | 67.9 ± 2.1 | −29.4 ± 0.1 |

[a]The binding stoichiometry $n$ is in terms of moles of DNA base pairs per mole of bound complex. The calculated binding free energy $\Delta G$ and binding entropy $\Delta S$ for the reaction are also shown.

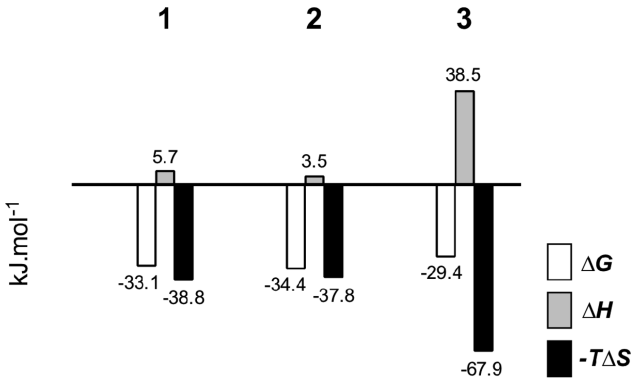


**Figure 8.** Enthalpic ($\Delta H$) and entropic ($-T\Delta S$) contributions to the Gibbs free energy ($\Delta G$) of **1**−**3** binding to CT-DNA.

taken into account for the analysis, being ∼20% at pH 6.0−6.5 and negligible at other pH values). The pH profile for the activity of both complexes is bell-shaped with an optimum at pH ∼7.0 (Figure 9).

The DNA cleavage efficiencies of **1** and **2** were assessed in terms of their concentrations (Figure 10). The two complexes reveal similar patterns of concentration-dependent DNA cleavage. In the range of 0.5−2.5 $\mu$M, **1** promotes only conversion of the supercoiled DNA fraction (F I) to the open circular form (F II), which represents a single-stranded scission event. Only at concentrations above 2.5 $\mu$M does **1** convert F I to F III, which represents a double-stranded cleavage event. Complex **2**, in contrast, is capable of double-stranded cleavage even at 2.5 $\mu$M.

In order to assess the effect of the pyrene groups in **1** and **2**, their DNA cleavage efficiencies were compared to that of **3**. At pH 7.0 and at a concentration of 5 $\mu$M, **3** promotes the cleavage of only ∼30% of the plasmid DNA, which is significantly lower than that cleaved by **1** or **2** (∼90−100%). This observation strongly suggests that the pyrene groups enhance DNA binding and, consequently, also DNA cleavage

In aqueous solutions at pH 7.0, plasmid DNA is a large polyanionic biopolymer. Under the same conditions, the amino groups within the 1,4-diaminobutane linker in complexes **1** and **2** are expected to be positively charged. It is thus possible that electrostatic interactions between the negatively charged DNA and the positively charged linkers play an important role in binding.

To probe this hypothesis, DNA cleavage reactions were performed with increasing concentrations of NaCl (50−500 mM) to modulate the ionic strength of the reaction medium. The increase in the ionic strength clearly reduces the activity toward plasmid DNA for both complexes (Figure S14A,B). The same result was obtained when assays were performed in the presence of $NaClO_4$ instead of NaCl (Figure S14C,D).

Because perchlorate ions are less likely to coordinate directly to the metal ions than the chloride ion, the results in Figure S14 are in agreement with electrostatic interactions contributing to

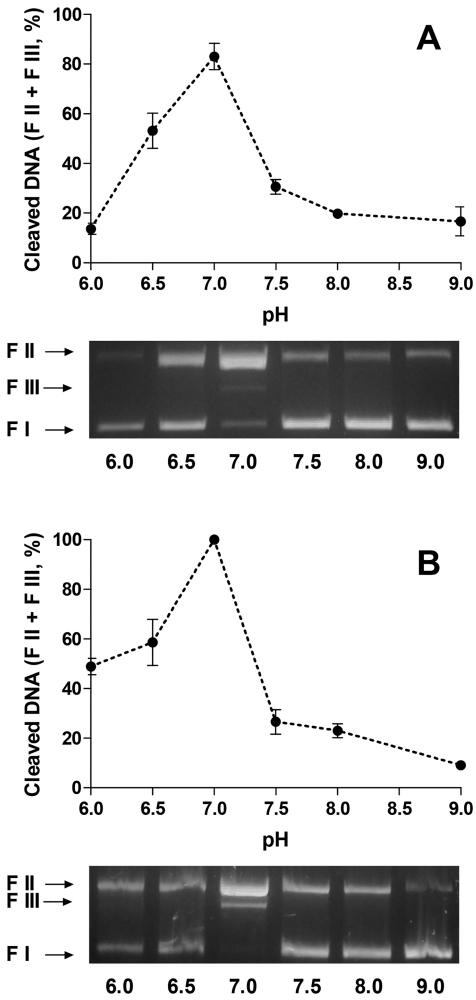


**Figure 9.** pH profile of plasmid DNA cleavage by 5 $\mu$M **1** (A) and **2** (B) for 16 h at 37 °C in a 10 mM buffer (MES, pH 6.0−6.5; HEPES, pH 7.0−8.0; CHES, pH 9.0). Results are expressed as mean value ± standard deviation obtained from three independent experiments.

the complex-mediated DNA cleavage process. However, these results do not rule out other types of complex/DNA interactions, such as groove binding. Thus, assays in the presence of the minor groove binder netropsin (50 $\mu$M) or the major groove binder methyl green (50 $\mu$M) were also performed (Figure S15). Both groove binders diminish the complex-promoted DNA cleavage, indicating that groove binding also contributes to the binding interactions between the substrate and catalysts. However, no groove binding preference or dependence was found because the two groove binders influence the cleavage activity to the same extent.

The mechanism of DNA strand scission was investigated by assessing the effect of ROS scavengers on the DNA cleavage efficiencies of **1** and **2** (Figure S16). None of the scavengers had a significant effect on the cleavage, suggesting that a hydrolytic


DOI: 10.1021/acs.inorgchem.7b02384
Inorg. Chem. XXXX, XXX, XXX−XXX

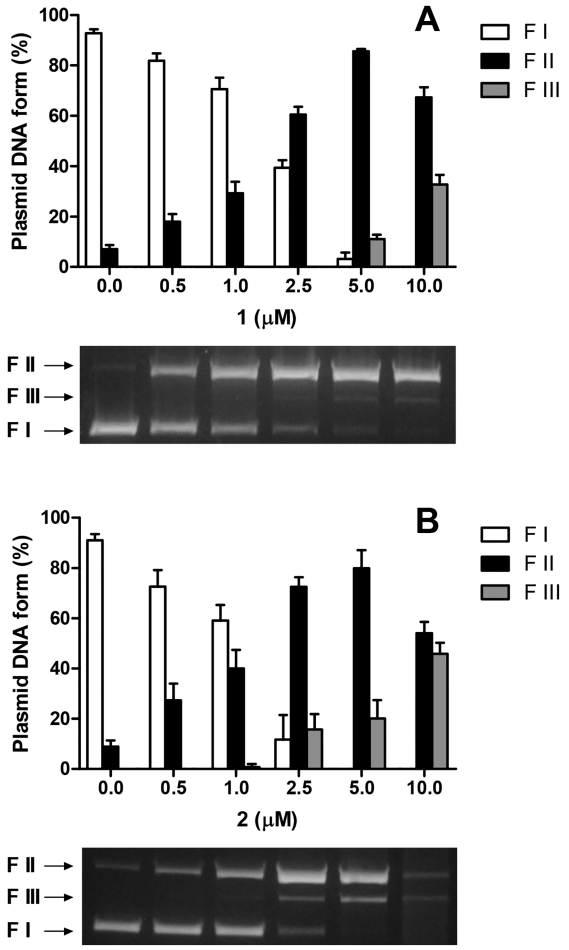


**Figure 10.** Complex concentration dependence of plasmid DNA cleavage by **1** (A) and **2** (B) for 16 h at 37 °C in 10 mM HEPES buffer (pH 7.0).

rather than oxidative pathway is associated with the ability of the complexes to promote DNA cleavage. The DNA cleavage mechanism was also investigated by monitoring the catalytic parameters of the reaction (Figure 11). Assays were conducted under pseudo-Michaelis–Menten conditions as described previously.[57] Complexes **1** and **2** induce DNA precipitation at concentrations higher than 10 $\mu$M (data not shown). Because of this limitation, the concentration of the complexes used in the experiments was 5 $\mu$M (Figure S16). Complex **2** is the most efficient system ($k_{obs}$ = 0.355 $h^{-1}$; $t_{1/2}$ = ~1.9 h), followed by **1**

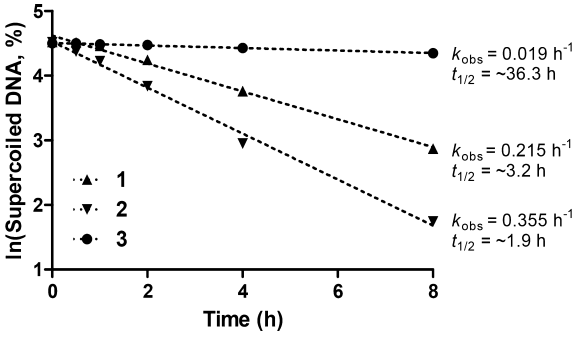


**Figure 11.** Kinetics of plasmid DNA cleavage by 5 $\mu$M **1**–**3** monitored over 8 h at 37 °C in a 10 mM HEPES buffer (pH 7.0). Measurements were carried out in duplicate.

($k_{obs}$ = 0.215 $h^{-1}$; $t_{1/2}$ = ~3.2 h). Compared to **3** ($k_{obs}$ = 0.019 $h^{-1}$; $t_{1/2}$ = ~36.3 h), the pyrene-modified systems **1** and **2** exhibit 11- and 19-fold higher activity, respectively. The combined results for the reactivity and mechanism of DNA cleavage suggest that the pyrene groups do not affect the mechanism of hydrolysis but instead enhance the binding of the catalysts. Similar results were observed for a diiron(III) complex, with the symmetrical dinucleating ligand 2,6-bis[(2-hydroxybenzyl)(2-pyridylmethyl)aminomethyl]-4-methylphenol ($H_3$L4) containing two linked acridine groups[15] or a pyrene.[58]

In an attempt to evaluate the binding preferences in terms of nucleotide sequence or structural DNA motifs, DNase I footprinting assays were performed with (**1**) – (**3**). It should be noted that none of the complexes was able to cleave the oligonucleotide substrate directly, and thus we were unable to detect cleavage of the fluorescent probe to establish the location of the target site (data not shown). On the other hand, DNase I protection assays were successful, as shown in Figure S17.

**DNase I Footprinting.** DNase I footprinting has been routinely used as a reliable assay to determine the DNA binding of several small organic compounds.[59] Although few studies on the DNase I footprinting of metal compounds have been reported,[60–62] this methodology can be used to identify the DNA binding sites of proteins and small molecules. In general, our DNase I footprinting assays revealed that the three complexes analyzed have distinct binding behaviors (Figure S17). Complex **3** binds preferentially at an AT-rich region covering four nucleotides from T9 to A12 (A, TTAA). Two other weak binding sites are located at C16–C17 (B) and C23–T24 (C). Complex **1** showed additional binding sites including an expanded binding site A up to T13 (TTAAT) and a fourth binding site (D, T41–A42, and A44) that is A, complementary to the A binding site, with an offset between + and – strands of three base pairs, which could be indicative of minor groove contacts. Finally, the complex **2** binding site is similar to that of **1**, with the addition of an expanded binding site B including G15 and G18–C20 (E, GCCGGC). The proposed binding sites for each complex are summarized in Figure 12. The presence of

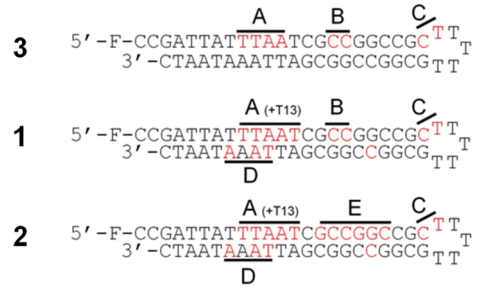


**Figure 12.** Proposed DNA binding sites of **3**, **1**, and **2** within the 49-mer oligonucleotide. Note that E refers to the expanded binding site B including a G15 and G18–C20. The nucleotides in red refer to the DNase I cleavage sites protected due to complex binding.

pyrene motifs in **1** and **2** apparently enhances the binding affinity of these compounds to DNA, as evidenced by the increase in the apparent binding strength for sites A/D and B (empirically evidenced by a strong inhibition of DNase I cleavage at these sites), and also expands the range and number of binding sites (Figure S17). Furthermore, the addition of pyrene increases the structural size of the complexes, affecting the number of nucleotides that can interact with **1** and **2** inside each binding site. Because pyrene behaves as a general intercalator, it can act as


DOI: 10.1021/acs.inorgchem.7b02384
Inorg. Chem. XXXX, XXX, XXX–XXX

a "chemical anchor", allowing **1** and **2** to interact with additional vicinal nucleotides.

**Cell Cytotoxicity.** Both complexes **1** and **3** are able to inhibit cellular growth in a concentration-dependent manner, with the $IC_{50}$ values indicated in Table 10. Apoptosis, a form of programmed cell death, is an important determinant of the response of tumor cells to chemotherapeutic agents. In apoptotic cells, phosphatidylserine is translocated from the inner to the outer leaflet of the plasma membrane. Annexin V can be used to identify apoptotic cells because it binds to exposed phosphatidylserine on the outer leaflet. Propidium iodide, a nucleic acid binding dye, is impermeable to live and apoptotic cells but stains dead cells with red fluorescence. The combination of the two dyes allows apoptotic cells (annexin V positive and propidium iodide negative), necrotic cells (double labeled with annexin V and propidium iodide), and viable cells (unmarked) to be differentiated.

**Table 10. $IC_{50}$ for Complexes 1 and 3**

| | $IC_{50}$ | |
|---|---|---|
| complex | 72 h | 24 h |
| **1** | 2.76 ± 0.30 | 6.52 ± 0.60 |
| **3** | 8.80 ± 0.90 | 18.76 ± 1.70 |

[a] $IC_{50}$ is the concentration ($\mu$M) required to inhibit 50% of K562 cell growth. The values are the mean of triplicate determinations.

At concentrations between 0.5 and 20 $\mu$M, complexes **1** and **3** induce cellular apoptosis in a concentration-dependent manner (Figure S18). The apoptotic effects of these two complexes are more pronounced than that of cisplatin. Following treatment with 10 $\mu$mol/L complex **1**, approximately 60% of the cells undergo apoptosis compared with 11% for complex **3** and only 5.3% for cisplatin. At the highest concentration tested (20 $\mu$M), only ~5% of the cells treated with complex **1** are viable, whereas ~50% of the cells treated with complex **3** remain unmarked (Figure S19). These results are in agreement with the $IC_{50}$ values determined in the cytotoxic assays. Furthermore, the necrotic effect of complex **3** and cisplatin is more pronounced than that of complex **1**, as shown by the percentage of cells stained with propidium iodide.

The strong fluorescence of complex **1** allowed an assessment of its intracellular location. Propidium iodide was used as a nucleic acid binding dye and lysotracker as a lysosome dye. The localization of **1** does not coincide with that of propidium iodide (last column in Figure 13), which means that the compound does not accumulate in the nucleus.

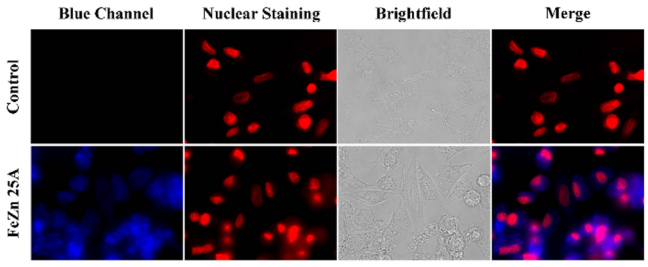


**Figure 13.** Cellular localization of compound **1** observed by fluorescence microscopy. The complex is pseudocolored in blue and the nuclear dye, propidium iodide, in red. In the last column (Merge), one can see that the localization of the compound does not coincide with that of the dye.

Confocal microscopic analysis of the nuclear epidermal growth factor receptor (EGFR) with nuclei of ameloblast-like cells (Figure 14) shows that complex **1** displays excellent colocalization with lysosomes. Lysosomes, which are cellular organelles found in all animal cells, play key roles in cellular metabolism, endocytosis, and the synthesis or assembly of hydrolases involved in macromolecule digestion. Various proteases regulate lysosomal trafficking and the intralysosomal pH.[49,63]

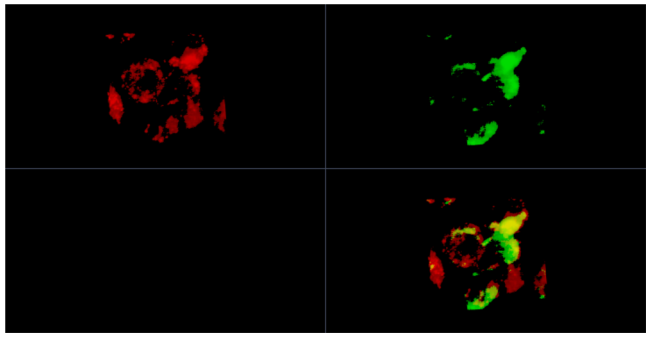

**Figure 14.** Accumulation in lysosomes. Confocal microscopic analysis showing colocalization of complex **1** with the lysotracker. Complex **1** is pseudocolored in green and the lysotracker in red. Incubation time = 5 h, and [**1**] = 80 $\mu$M. Original magnification: 63×.

Lysosome dysfunction has been implicated in the invasion, metastasis, and maintenance of cancerous tissues.[64] Lysosome membrane permeabilization can induce cell death because the release of lysosomal proteases in the cytosol causes the digestion of vital proteins and the activation of additional hydrolases including caspases.[65,66] Partial lysosomal permeabilization occurs in several models of apoptosis, a phenomenon known as the "lysosomal pathway of apoptosis". A large number of potential anticancer drugs induce p53-independent apoptosis mediated by partial lysosomal permeabilization, suggesting that these pathways are potential targets for anticancer drug development.[67]

Platinum compounds with antitumor properties, such as a fluorophore-labeled cisplatin, were also localized in lysosomal compartments.[68,69] A series of luminescent platinum(II) complexes containing pincer-type ligands with pyrazole moieties also accumulates in the lysosomes of cancer cells, increasing the lysosomal membrane permeability and inducing cell death.[70] Thus, the enhanced apoptotic effect of **1**, together with its colocalization in lysosomes, indicates that this compound is an excellent lead for novel anticancer drugs.

## CONCLUSIONS

In summary, we have synthesized and characterized two new dinuclear $Fe^{III}Zn^{II}$ hydrolase biomimetics **1** and **2**, in which the carbonyl group in the ligand L1 was modified to contain one ($H_2$LP1) or two ($H_2$LP2) pyrene groups conjugated to the dinucleating ligand by a 1,4-diaminobutane spacer. The diesterase activity (using the model substrate BDNPP and DNA) and cytotoxic activity (estimated by the corresponding $IC_{50}$ values) of **1** and **2** are significantly increased in comparison to their parental counterpart, i.e., the $[Fe^{III}Zn^{II}L1]$ (**3**) complex, because of the presence of protonated amines and conjugated pyrene group(s), which exert second-coordination-sphere effects on the catalytic efficiency of these species. Interestingly, confocal fluorescence microscopy analysis of the nuclear EGFR with nuclei of ameloblast-like cells shows that complex **1** displays excellent colocalization with lysosomes and does not seem to


DOI: 10.1021/acs.inorgchem.7b02384
Inorg. Chem. XXXX, XXX, XXX−XXX

accumulate in the nucleus of the cell. Further studies involving variations in the side-chain length (ethyl, propyl, and hexyl), as well as in the intercalating group are underway and will be the subject of further reports.

## ■ ASSOCIATED CONTENT

### Supporting Information

The Supporting Information is available free of charge on the ACS Publications website at DOI: 10.1021/acs.inorgchem.7b02384.

Synthesis of the ligands $H_2$LP1 and $H_2$LP2 (Schemes S1 and S2), characterization of the ligands and their complexes **1** and **2** (Figures S1−S10), kinetics (Figure S11), DNA interaction of **1** and **2** (Figures S12−S17), and cell interaction (Figures S18 and S19) (PDF)

## ■ AUTHOR INFORMATION


### Corresponding Authors

*E-mail: ademir.neves@ufsc.br. Phone: +55 (48) 3721-3605.
*E-mail: hernan.terenzi@ufsc.br.

### ORCID

Ademir Neves: 0000-0002-6713-798X
Rosely A. Peralta: 0000-0002-6417-2683


### Author Contributions

The manuscript was written with contributions from all authors. All authors have approved the final version of the manuscript.

### Notes

The authors declare no competing financial interest.

## ■ ACKNOWLEDGMENTS

Financial support was received from CNPq, CAPES, FAPESC, and INCT-catalise (Brazil). G.S. acknowledges the Australian Research Council for the award of a Future Fellowship (FT120100694).

## ■ REFERENCES


(1) Piovezan, C.; Jovito, R.; Bortoluzzi, A. J.; Terenzi, H.; Fischer, F. L.; Severino, P. C.; Pich, C. T.; Azzolini, G. G.; Peralta, R. A.; Rossi, L. M.; Neves, A. Heterodinuclear $Fe^{III}Zn^{II}$-Bioinspired Complex Supported on 3-Aminopropyl Silica. Efficient Hydrolysis of Phosphate Diester Bonds. *Inorg. Chem.* **2010**, *49*, 2580−2582.

(2) Desbouis, D.; Troitsky, I. P.; Belousoff, M. J.; Spiccia, L.; Graham, B. Copper(II), zinc(II) and nickel(II) complexes as nuclease mimetics. *Coord. Chem. Rev.* **2012**, *256*, 897−937.

(3) Mancin, F.; Scrimin, P.; Tecilla, P. Progress in artificial metallonucleases. *Chem. Commun.* **2012**, *48*, 5545−5559.

(4) Mitić, N.; Smith, S. J.; Neves, A.; Guddat, L. W.; Gahan, L. R.; Schenk, G. The Catalytic Mechanisms of Binuclear Metallohydrolases. *Chem. Rev.* **2006**, *106*, 3338−3363.

(5) Zhao, M.; Wang, H.-B.; Ji, L.-N.; Mao, Z.-W. Insights into metalloenzyme microenvironments: biomimetic metal complexes with a functional second coordination sphere. *Chem. Soc. Rev.* **2013**, *42*, 8360−8375.

(6) Rebilly, J.-N.; Colasson, B.; Bistri, O.; Over, D.; Reinaud, O. Biomimetic cavity-based metal complexes. *Chem. Soc. Rev.* **2015**, *44*, 467−489.

(7) de Souza, B.; Kreft, G. L.; Bortolotto, T.; Terenzi, H.; Bortoluzzi, A. J.; Castellano, E. E.; Peralta, R. A.; Domingos, J. B.; Neves, A. Second-Coordination-Sphere Effects Increase the Catalytic Efficiency of an Extended Model for $Fe^{III}M^{II}$ Purple Acid Phosphatases. *Inorg. Chem.* **2013**, *52*, 3594−3596.

(8) de Souza, B.; Heying, R.; Bortoluzzi, A. J.; Domingos, J. B.; Neves, A. The effect of chain size on the modeling of second sphere effects in biomimetic complexes. *J. Mol. Catal. A: Chem.* **2015**, *397*, 76−84.

(9) Kövári, E.; Krämer, R. Rapid Phosphodiester Hydrolysis by an Ammonium-Functionalized Copper(II) Complex. A Model for the Cooperativity of Metal Ions and NH-Acidic Groups in Phosphoryl Transfer Enzymes. *J. Am. Chem. Soc.* **1996**, *118*, 12704−12709.

(10) Comba, P.; Gahan, L. R.; Hanson, G. R.; Mereacre, V.; Noble, C. J.; Powell, A. K.; Prisecaru, I.; Schenk, G.; Zajaczkowski-Fischer, M. Monoesterase Activity of a Purple Acid Phosphatase Mimic with a Cyclam Platform. *Chem. - Eur. J.* **2012**, *18*, 1700−1710.

(11) Kendall, A. J.; Zakharov, L. N.; Gilbertson, J. D. Synthesis and Stabilization of a Monomeric Iron(II) Hydroxo Complex via Intramolecular Hydrogen Bonding in the Secondary Coordination Sphere. *Inorg. Chem.* **2010**, *49*, 8656−8658.

(12) Basile, L. A.; Barton, J. K. Design of a double-stranded DNA cleaving agent with two polyamine metal-binding arms: Ru(DIP)$_2$Macron$^+$. *J. Am. Chem. Soc.* **1987**, *109*, 7548−7550.

(13) Rammo, J.; Hettich, R.; Roigk, A.; Schneider, H.-J. Catalysis of DNA cleavage by lanthanide complexes with nucleophilic or intercalating ligands and their kinetic characterization. *Chem. Commun.* **1996**, *1*, 105−107.

(14) Sissi, C.; Rossi, P.; Felluga, F.; Formaggio, F.; Palumbo, M.; Tecilla, P.; Toniolo, C.; Scrimin, P. Dinuclear $Zn^{2+}$ Complexes of Synthetic Heptapeptides as Artificial Nucleases. *J. Am. Chem. Soc.* **2001**, *123*, 3169−3170.

(15) Chen, X.; Fan, J.; Peng, X.; Wang, J.; Sun, S.; Zhang, R.; Wu, T.; Zhang, F.; Liu, J.; Wang, F.; Ma, S. Bisintercalator-containing dinuclear iron(III) complex: An efficient artificial nuclease. *Bioorg. Med. Chem. Lett.* **2009**, *19*, 4139−4142.

(16) Boseggia, E.; Gatos, M.; Lucatello, L.; Mancin, F.; Moro, S.; Palumbo, M.; Sissi, C.; Tecilla, P.; Tonellato, U.; Zagotto, G. Toward Efficient Zn(II)-Based Artificial Nucleases. *J. Am. Chem. Soc.* **2004**, *126*, 4543−4549.

(17) Gahan, L. R.; Smith, S. J.; Neves, A.; Schenk, G. Phosphate Ester Hydrolysis: Metal Complexes As Purple Acid Phosphatase and Phosphotriesterase Analogues. *Eur. J. Inorg. Chem.* **2009**, *2009*, 2745−2758.

(18) Xavier, F. R.; Peralta, R. A.; Bortoluzzi, A. J.; Drago, V.; Castellano, E. E.; Haase, W.; Tomkowicz, Z.; Neves, A. Bioinspired $Fe^{III}Cd^{II}$ and $Fe^{III}Hg^{II}$ complexes: Synthesis, characterization and promiscuous catalytic activity evaluation. *J. Inorg. Biochem.* **2011**, *105*, 1740−1752.

(19) Schenk, G.; Peralta, R.; Batista, S.; Bortoluzzi, A.; Szpoganicz, B.; Dick, A.; Herrald, P.; Hanson, G.; Szilagyi, R.; Riley, M.; Gahan, L.; Neves, A. Probing the role of the divalent metal ion in uteroferrin using metal ion replacement and a comparison to isostructural biomimetics. *JBIC, J. Biol. Inorg. Chem.* **2007**, *13*, 139−155.

(20) Peralta, R. A.; Bortoluzzi, A. J.; de Souza, B.; Jovito, R.; Xavier, F. R.; Couto, R. A. A.; Casellato, A.; Nome, F.; Dick, A.; Gahan, L. R.; Schenk, G.; Hanson, G. R.; de Paula, F. C. S.; Pereira-Maia, E. C.; de P. Machado, S.; Severino, P. C.; Pich, C.; Bortolotto, T.; Terenzi, H.; Castellano, E. E.; Neves, A.; Riley, M. J. Electronic Structure and Spectro-Structural Correlations of $Fe^{III}Zn^{II}$ Biomimetics for Purple Acid Phosphatases: Relevance to DNA Cleavage and Cytotoxic Activity. *Inorg. Chem.* **2010**, *49*, 11421−11438.

(21) Neves, A.; Lanznaster, M.; Bortoluzzi, A. J.; Peralta, R. A.; Casellato, A.; Castellano, E. E.; Herrald, P.; Riley, M. J.; Schenk, G. An Unprecedented $Fe^{III}(\mu$-OH)$Zn^{II}$ Complex that Mimics the Structural and Functional Properties of Purple Acid Phosphatases. *J. Am. Chem. Soc.* **2007**, *129*, 7486−7487.

(22) Smith, S. J.; Peralta, R. A.; Jovito, R.; Horn, A.; Bortoluzzi, A. J.; Noble, C. J.; Hanson, G. R.; Stranger, R.; Jayaratne, V.; Cavigliasso, G.; Gahan, L. R.; Schenk, G.; Nascimento, O. R.; Cavalett, A.; Bortolotto, T.; Razzera, G.; Terenzi, H.; Neves, A.; Riley, M. J. Spectroscopic and Catalytic Characterization of a Functional $Fe^{III}Fe^{II}$ Biomimetic for the Active Site of Uteroferrin and Protein Cleavage. *Inorg. Chem.* **2012**, *51*, 2065−2078.

(23) Lanznaster, M.; Neves, A.; Bortoluzzi, A. J.; Aires, V. V. E.; Szpoganicz, B.; Terenzi, H.; Severino, P. C.; Fuller, J. M.; Drew, S. C.; Gahan, L. R.; Hanson, G. R.; Riley, M. J.; Schenk, G. A new heterobinuclear $Fe^{III}Cu^{II}$ complex with a single terminal $Fe^{III}$−




DOI: 10.1021/acs.inorgchem.7b02384
*Inorg. Chem.* XXXX, XXX, XXX−XXX

O(phenolate) bond. Relevance to purple acid phosphatases and nucleases. *JBIC, J. Biol. Inorg. Chem.* **2005**, *10*, 319−332.
(24) Smith, S. J.; Casellato, A.; Hadler, K. S.; Mitić, N.; Riley, M. J.; Bortoluzzi, A. J.; Szpoganicz, B.; Schenk, G.; Neves, A.; Gahan, L. R. The reaction mechanism of the Ga(III)Zn(II) derivative of uteroferrin and corresponding biomimetics. *JBIC, J. Biol. Inorg. Chem.* **2007**, *12*, 1207−1220.
(25) Ausubel, F. M.; Brent, R.; Kingston, R. E.; Moore, D. D.; Seidman, J. G.; Smith, J. A.; Struhl, K. *Short Protocols in Molecular Biology: A Compendium of Methods from Current Protocols in Molecular Biology*, 4th ed.; Wiley: New York, 1999.
(26) Rock, P. A. The Standard Oxidation Potential of the Ferrocyanide-Ferricyanide Electrode at 25° and the Entropy of Ferrocyanide Ion. *J. Phys. Chem.* **1966**, *70*, 576−580.
(27) Strohalm, M.; Kavan, D.; Novák, P.; Volný, M.; Havlíček, V. mMass 3: A Cross-Platform Software Environment for Precise Analysis of Mass Spectrometric Data. *Anal. Chem.* **2010**, *82*, 4648−4651.
(28) Barbosa, J.; Sanz-Nebot, V. Autoprotolysis constants and standardization of the glass electrode in acetonitrile-water mixtures. Effect of solvent composition. *Anal. Chim. Acta* **1991**, *244*, 183−191.
(29) Martell, A. E.; Montekaitis, R. J. *Determination and use of stability constants*, 2nd ed.; VCD: New York, 1992.
(30) George, G. N. *EXAFSPAK and EDG-FIT*; Stanford Synchrotron Radiation Laboratory: Stanford, CA, 2000.
(31) Rehr, J. J.; Kas, J. J.; Vila, F. D.; Prange, M. P.; Jorissen, K. Parameter-free calculations of X-ray spectra with FEFF9. *Phys. Chem. Chem. Phys.* **2010**, *12*, 5503−5513.
(32) Tierney, D. L.; Schenk, G. X-Ray Absorption Spectroscopy of Dinuclear Metallohydrolases. *Biophys. J.* **2014**, *107*, 1263−1272.
(33) Wiseman, T.; Williston, S.; Brandts, J. F.; Lin, L.-N. Rapid measurement of binding constants and heats of binding using a new titration calorimeter. *Anal. Biochem.* **1989**, *179*, 131−137.
(34) Holde, K. E. v.; Johnson, C.; Ho, P. S. *Principles of Physical Biochemistry*, 2nd ed.; Prentice Hall: Upper Saddle River, NJ, 2006.
(35) Grossoehme, N.; Spuches, A.; Wilcox, D. Application of isothermal titration calorimetry in bioinorganic chemistry. *JBIC, J. Biol. Inorg. Chem.* **2010**, *15*, 1183−1191.
(36) Pedroso, M. M.; Ely, F.; Mitić, N.; Carpenter, M. C.; Gahan, L. R.; Wilcox, D. E.; Larrabee, J. L.; Ollis, D. L.; Schenk, G. Comparative investigation of the reaction mechanisms of the organophosphate-degrading phosphotriesterases from Agrobacterium radiobacter (OpdA) and Pseudomonas diminuta (OPH). *JBIC, J. Biol. Inorg. Chem.* **2014**, *19*, 1263−1275.
(37) Cooper, A.; Johnson, C. In *Microscopy, Optical Spectroscopy, and Macroscopic Techniques*; Jones, C., Mulloy, B., Thomas, A., Eds.; Humana Press, 1994; Vol. *22*, Chapter 9, pp 109−124.
(38) Ladbury, J. E.; Chowdhry, B. Z. Sensing the heat: the application of isothermal titration calorimetry to thermodynamic studies of biomolecular interactions. *Chem. Biol.* **1996**, *3*, 791−801.
(39) Mancin, F.; Scrimin, P.; Tecilla, P.; Tonellato, U. Artificial metallonucleases. *Chem. Commun.* **2005**, 2540−2548.
(40) Muxel, A. A.; Neves, A.; Camargo, M. A.; Bortoluzzi, A. J.; Szpoganicz, B.; Castellano, E. E.; Castilho, N.; Bortolotto, T.; Terenzi, H. New La(III) Complex Immobilized on 3-Aminopropyl-Functionalized Silica as an Efficient and Reusable Catalyst for Hydrolysis of Phosphate Ester Bonds. *Inorg. Chem.* **2014**, *53*, 2943−2952.
(41) Bernadou, J.; Pratviel, G.; Bennis, F.; Girardet, M.; Meunier, B. Potassium monopersulfate and a water-soluble manganese porphyrin complex, [Mn(TMPyP)](OAc)$_5$, as an efficient reagent for the oxidative cleavage of DNA. *Biochemistry* **1989**, *28*, 7268−7275.
(42) Van Dyke, M. W.; Hertzberg, R. P.; Dervan, P. B. Map of distamycin, netropsin, and actinomycin binding sites on heterogeneous DNA: DNA cleavage-inhibition patterns with methidiumpropyl-EDTA.Fe(II). *Proc. Natl. Acad. Sci. U. S. A.* **1982**, *79*, 5470−5474.
(43) Silva, P. P.; Guerra, W.; Silveira, J. N.; Ferreira, A. M. d. C.; Bortolotto, T.; Fischer, F. L.; Terenzi, H.; Neves, A.; Pereira-Maia, E. C. Two New Ternary Complexes of Copper(II) with Tetracycline or Doxycycline and 1,10-Phenanthroline and Their Potential as Antitumoral: Cytotoxicity and DNA Cleavage. *Inorg. Chem.* **2011**, *50*, 6414−6424.
(44) Roe, A. L.; Schneider, D. J.; Mayer, R. J.; Pyrz, J. W.; Widom, J.; Que, L. X-ray absorption spectroscopy of iron-tyrosinate proteins. *J. Am. Chem. Soc.* **1984**, *106*, 1676−1681.
(45) Kruve, A.; Kaupmees, K.; Liigand, J.; Oss, M.; Leito, I. Sodium adduct formation efficiency in ESI source. *J. Mass Spectrom.* **2013**, *48*, 695−702.
(46) Schenk, G.; Mitić, N.; Hanson, G. R.; Comba, P. Purple acid phosphatase: A journey into the function and mechanism of a colorful enzyme. *Coord. Chem. Rev.* **2013**, *257*, 473−482.
(47) Cox, B. G. *Acids and Bases: Solvent Effects on Acid−base strength*; Oxford University Press: Oxford, U.K., 2013.
(48) Winnik, F. M. Photophysics of preassociated pyrenes in aqueous polymer solutions and in other organized media. *Chem. Rev.* **1993**, *93*, 587−614.
(49) Comba, P.; Gahan, L. R.; Mereacre, V.; Hanson, G. R.; Powell, A. K.; Schenk, G.; Zajaczkowski-Fischer, M. Spectroscopic Characterization of the Active $Fe^{III}Fe^{III}$ and $Fe^{III}FeII$ Forms of a Purple Acid Phosphatase Model System. *Inorg. Chem.* **2012**, *51*, 12195−12209.
(50) Deal, K. A.; Hengge, A. C.; Burstyn, J. N. Characterization of Transition States in Dichloro(1,4,7-triazacyclononane)copper(II)-Catalyzed Activated Phosphate Diester Hydrolysis. *J. Am. Chem. Soc.* **1996**, *118*, 1713−1718.
(51) Bunton, C. A.; Farber, S. J. Hydrolysis of bis(2,4-dinitrophenyl) phosphate. *J. Org. Chem.* **1969**, *34*, 767−772.
(52) Sunita, M.; Anupama, B.; Ushaiah, B.; Gyana Kumari, C. Synthesis, characterization, DNA binding and cleavage studies of mixed-ligand copper (II) complexes. *Arabian J. Chem.* **2017**, *10*, S3367−S3374.
(53) Pages, B. J.; Ang, D. L.; Wright, E. P.; Aldrich-Wright, J. R. Metal complex interactions with DNA. *Dalton Trans.* **2015**, *44*, 3505−3526.
(54) Haq, I.; Lincoln, P.; Suh, D.; Norden, B.; Chowdhry, B. Z.; Chaires, J. B. Interaction of.DELTA.- and.LAMBDA.-[Ru(phen)$_2$DPPZ]$^{2+}$ with DNA: A Calorimetric and Equilibrium Binding Study. *J. Am. Chem. Soc.* **1995**, *117*, 4788−4796.
(55) Li, L.-Y.; Jia, H.-N.; Yu, H.-J.; Du, K.-J.; Lin, Q.-T.; Qiu, K.-Q.; Chao, H.; Ji, L.-N. Synthesis, characterization, and DNA-binding studies of ruthenium complexes [Ru(tpy)(ptn)]$^{2+}$ and Ru(dmtpy)(ptn)]$^{2+}$. *J. Inorg. Biochem.* **2012**, *113*, 31−39.
(56) Kuntz, I. D.; Chen, K.; Sharp, K. A.; Kollman, P. A. The maximal affinity of ligands. *Proc. Natl. Acad. Sci. U. S. A.* **1999**, *96*, 9997−10002.
(57) Sreedhara, A.; Freed, J. D.; Cowan, J. A. Efficient Inorganic Deoxyribonucleases. Greater than 50-Million-Fold Rate Enhancement in Enzyme-Like DNA Cleavage. *J. Am. Chem. Soc.* **2000**, *122*, 8814−8824.
(58) Chen, X. Q.; Wang, J. Y.; Zhang, T. Y.; Zhang, L. Z.; Peng, X. J. Synthesis and DNA cleavage activity of diiron(III) complex bearing pyrene group. *Chin. Chem. Lett.* **2008**, *19*, 342−344.
(59) Bailly, C.; Denny, W. A.; Mellor, L. E.; Wakelin, L. P. G.; Waring, M. J. Sequence specificity of the binding of 9-aminoacridine- and amsacrine-4-carboxamides to DNA studied by DNase I footprinting. *Biochemistry* **1992**, *31*, 3514−3524.
(60) Rüba, E.; Hart, J. R.; Barton, J. K. [Ru(bpy)$_2$(L)]Cl$_2$: Luminescent Metal Complexes That Bind DNA Base Mismatches. *Inorg. Chem.* **2004**, *43*, 4570−4578.
(61) Kikuta, E.; Aoki, S.; Kimura, E. New potent agents binding to a poly(dT) sequence in double-stranded DNA: bis($Zn^{2+}$-cyclen) and tris($Zn^{2+}$-cyclen) complexes. *JBIC, J. Biol. Inorg. Chem.* **2002**, *7*, 473−482.
(62) Chválová, K.; Kašpárková, J.; Farrell, N.; Brabec, V. Deoxyribonuclease I footprinting reveals different DNA binding modes of bifunctional platinum complexes. *FEBS J.* **2006**, *273*, 3467−3478.
(63) Yapici, N. B.; Bi, Y.; Li, P.; Chen, X.; Yan, X.; Mandalapu, S. R.; Faucett, M.; Jockusch, S.; Ju, J.; Gibson, K. M.; Pavan, W. J.; Bi, L. Highly Stable and Sensitive Fluorescent Probes (LysoProbes) for Lysosomal Labeling and Tracking. *Sci. Rep.* **2015**, *5*, 8576.
(64) Koblinski, J. E.; Ahram, M.; Sloane, B. F. Unraveling the role of proteases in cancer. *Clin. Chim. Acta* **2000**, *291*, 113−135.


DOI: 10.1021/acs.inorgchem.7b02384
*Inorg. Chem.* XXXX, XXX, XXX−XXX

(65) Guicciardi, M. E.; Leist, M.; Gores, G. J. Lysosomes in cell death. *Oncogene* **2004**, *23*, 2881−2890.
(66) Boya, P.; Kroemer, G. Lysosomal membrane permeabilization in cell death. *Oncogene* **2008**, *27*, 6434−6451.
(67) Erdal, H.; Berndtsson, M.; Castro, J.; Brunk, U.; Shoshan, M. C.; Linder, S. Induction of lysosomal membrane permeabilization by compounds that activate p53-independent apoptosis. *Proc. Natl. Acad. Sci. U. S. A.* **2005**, *102*, 192−197.
(68) Molenaar, C.; Teuben, J.-M.; Heetebrij, R. J.; Tanke, H. J.; Reedijk, J. New insights in the cellular processing of platinum antitumor compounds, using fluorophore-labeled platinum complexes and digital fluorescence microscopy. *JBIC, J. Biol. Inorg. Chem.* **2000**, *5*, 655−665.
(69) Safaei, R.; Katano, K.; Larson, B. J.; Samimi, G.; Holzer, A. K.; Naerdemann, W.; Tomioka, M.; Goodman, M.; Howell, S. B. Intracellular Localization and Trafficking of Fluorescein-Labeled Cisplatin in Human Ovarian Carcinoma Cells. *Clin. Cancer Res.* **2005**, *11*, 756−767.
(70) Tsai, J. L.-L.; Zou, T.; Liu, J.; Chen, T.; Chan, A. O.-Y.; Yang, C.; Lok, C.-N.; Che, C.-M. Luminescent platinum(ii) complexes with self-assembly and anti-cancer properties: hydrogel, pH dependent emission color and sustained-release properties under physiological conditions. *Chem. Sci.* **2015**, *6*, 3823−3830.



DOI: 10.1021/acs.inorgchem.7b02384
*Inorg. Chem.* XXXX, XXX, XXX−XXX